CONSTRAINING THE DENSITY DEPENDENCE OF THE SYMMETRY ENERGY WITH EXPERIMENTAL RESULTS FROM HEAVY-ION COLLISIONS

Marie-France Rivet

CONSTRAINING THE DENSITY DEPENDENCE OF THE SYMMETRY ENERGY WITH EXPERIMENTAL RESULTS FROM HEAVY-ION COLLISIONS

MARIE-FRANCE RIVET

January 27, 2010

Institut de Physique Nucléaire,
91406 Orsay, France

Abstract

The equation of state of asymmetric nuclear matter is still controversial, as predictions at subsaturation as well as above-normal density diverge widely. We discuss in this lecture several experimental observables measured in heavy-ion collisions in the energy range 20-400 A MeV. Estimates of the density dependence of the symmetry energy are derived from comparison of experimental results with those of transport codes with different implementatiosn of the potential part of the symmetry energy, or in statistical model frameworks.

Contents

1 Introduction

The knowledge of the density dependence of the nuclear symmetry energy, E_{sym}, is critical in many areas of nuclear physics and astrophysics. At densities lower than saturation density, symmetry energy influences neutron skin, pigmy resonance, nuclear structure at the drip line. In heavy ion collisions it governs the competition between dissipative mechanisms, and manifests itself through neutron distillation in fragmentation, which is a signature of a phase transition. In astrophysics new observations on neutron stars have stimulated interest on the role of the symmetry energy in their formation, the structure of the crust (low density region), the mass-radius relation (high density core), up to the formation of black holes

In our terrestrial laboratories, heavy-ion collisions at and above Fermi energy provide the only way to explore densities different from the saturation density, ρ_0, as in the course of such a collision matter suffers compression and expansion phases. Several observables which should be sensitive to the symmetry energy have been proposed by theoreticians (for reviews, see [1, 2]), and the experimental search for measurable effects started some years ago with stable-isotope beams and targets spanning the largest possible N/Z range. The values and the evolution with density of the symmetry energy which can be derived from the experiments rely on models, generally transport codes simulating nuclear

collisions, or sometimes statistical models which are claimed to give the absolute value of the symmetry energy in given density and temperature conditions. Note that in both formalisms one deals at the end with hot nuclei that must be de-excited before any comparison with experimental data [1]. Up to now no de-excitation code has proven to be reliable for nuclei at high excitation energy (~ 3 AMeV). Moreover no constraining data exist when the excited nuclei are far from stability.

At normal density and zero temperature, a first determination of E_{sym} can be obtained from fits of nuclear binding energies with the liquid drop mass formula:

$$E(N,Z) = -a_V A + a_S A^{2/3} + a_{sym}\frac{(N-Z)^2}{A} + a_C\frac{Z^2}{A^{1/3}}$$

Except for light nuclei the nuclear energy is dominated by the volume term, responsible for nuclear binding, that the surface, symmetry and Coulomb terms tend to reduce. This formula and the derived symmetry energy is scrutinized in [3]. When fitting on more than 3000 nuclei with mass larger than 10, the symmetry energy coefficient a_{sym} takes a value of 22.5 MeV.

Considering that a nucleus has a bulk part at nearly constant density surrounded by a surface with decreasing density, one may wonder if the symmetry term of the nuclear mass should be divided into a volume and a surface part, in other terms if the coefficient a_{sym} should be mass dependent. This hypothesis was retained for instance in the droplet model [4, 5]. However due to the large number of parameters in this model, the values of the surface symmetry coefficient were found to vary by factors as large as 2. Therefore at the present time no conclusion can be obtained from the fit of nuclear masses. It is however concluded in [3] that *surface symmetry-energy emerges, as an unavoidable ingredient of the net nuclear energy, from simultaneous considerations of nuclear surface and symmetry energy.*

2 Symmetry energy and Statistical framework

Statistical models are based on a multi-body phase space description. They use the formalisms of equilibrium statistical mechanics. In this framework the collision stage of nuclear collisions is not considered, there is no time evolution. A system is considered in a "freeze-out" stage defined as the instant when the different products emerging from the reaction interact only through the Coulomb force, the nuclear interaction is considered as negligible. The fragments are assumed to have a spherical shape and the saturation density, ρ_0. It is important to stress that the concept of statistical equilibrium can certainly not be applied to the result of a single collision. One should define experimental statistical ensembles as a collection of events with similar properties, in order to sufficiently explore the available phase space. Another point to consider is that nuclear physicists are dealing with *finite systems*, which made it necessary to redefine the concepts long used at the thermodynamic limit, for infinite systems [6, 7].

2.1 Statistical ensembles

Three types of ensembles are used in statistical models. Whereas they give the same results at the thermodynamic limit, they present differences when used for finite systems.

- microcanonical: with fixed total energy and particle number, it appears as the most appropriate to describe isolated finite systems like nuclei. Among the most popular are the Microcanonical Metropolis Monte Carlo (MMMC) [8], the Microcanonical Multifragmentation Model (MMM) [9, 10], and the various implementations of the Statistical Multifragmentation Model (SMM) [11].

[1] A nuclear collision has a duration of the order of $10^{-22} - 10^{-21}$ s while its broken pieces are collected in detectors after $10^{-8} - 10^{-7}$ s

- canonical: it describes a system with a fixed number of nucleons, A, which can exchange energy with a reservoir at fixed temperature, T. The energy of the system thus fluctuates around a fixed mean value, with a standard deviation $\sigma_E = 4E/\sqrt{AT}$ [2] (within the Fermi gas model). This ensemble provides a reasonable approximation for nuclei $A \geq$200 and $T \geq 6$ MeV.

- grandcanonical: in that case the system can exchange energy and particles with a reservoir at temperature T. Only average values are constrained. In nuclear physics it becomes meaningful for nuclei at large excitation energies, when only mean values are considered.

2.2 Iso(tope)scaling

Ten years ago, the isoscaling properties of fragments produced in various types of nuclear processes drove a great interest [12]. The isotopic scaling, contracted in isoscaling, was observed when comparing the isotopic distributions of fragments produced in nuclear reactions between two systems differing only by their mass, with $A(2) > A(1)$. It was found that the yields $Y(N,Z)$ of produced nuclei obey the law:

$$\frac{Y_2(N,Z)}{Y_1(N,Z)} = C \exp\left[\alpha N + \beta Z\right] \tag{1}$$

the parameters α and β being the same for all light isotopes (Z<10). An example is shown in fig 1, with the expressions:

$$S(N) = \frac{Y_2(N,Z)}{Y_1(N,Z)} \exp -\beta Z \text{ and } S(Z) = \frac{Y_2(N,Z)}{Y_1(N,Z)} \exp -\alpha N,$$

defining the r.h.s. plots. Fragments in this case were produced in central collisions, selected by high total multiplicity values, in which multifragmentation of a system containing about 75% of the total mass, charge and energy occurs[13]. The conditions for the occurrence of isoscaling is that the systems

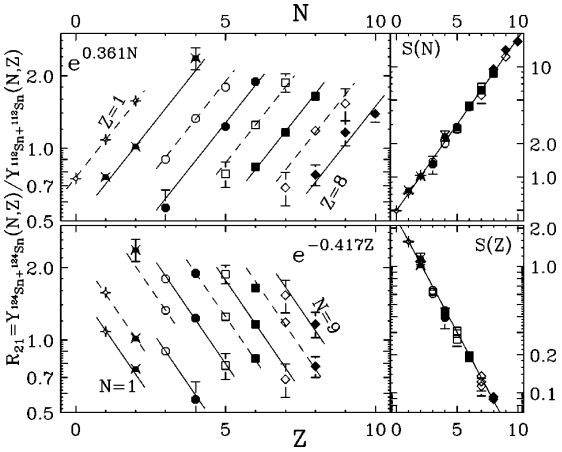

Figure 1: Nuclei yield ratios as a function of N (top panels) or Z (bottom panels) for central ^{124}Sn+^{124}Sn and ^{112}Sn+^{112}Sn collisions at E/A=50 MeV. The lines correspond to best fits with eq.1. From [14]

can be described by a statistical process and have the same temperature [14].

Indeed, in a grandcanonical framework, the isotopic yield for a fragment reads:

$$Y^{(i)}(A,Z) = \exp\left(\frac{1}{T^{(i)}}(-G(N,Z) + \mu_N^{(i)} N + \mu_Z^{(i)} Z)\right), \tag{2}$$

[2] with $a = A/8$; the more general expression is $\sigma_E = E \times \sqrt{2/aT}$, a being the level density parameter

μ_N and μ_Z being the neutron and proton chemical potentials and $G(N,Z)$ the free energy. Using this relation for two systems at same temperature, it can be seen that the isoscaling relation is satisfied with $\alpha = (\mu_N^{(2)} - \mu_N^{(1)})/T$. It was demonstrated in [15] that isoscaling is also predicted by canonical and microcanonical models.

What is the connection between isoscaling and the symmetry energy ? Let us turn back to the fragment yield expressed by Eq.2. For a given Z, taking into account that the range of N is limited, the free energy dependence on N can be approximated by:

$$G(N,Z) = a(Z) + c_0(Z)N + C_{sym}(Z)(N-Z)^2/A;$$

the last term can be regarded as the symmetry energy. The most probable value for each system, $\langle N\rangle(Z)$ is:

$$C_{sym}(Z)\left\{1 - 4[Z/\langle A\rangle(Z)]^2\right\} = \mu_N^{(i)} - a(Z)$$

Finally, subtracting system (1) from system (2) one obtains:

$$4C_{sym}(Z)/T = \alpha/\left[\left(\frac{Z}{\langle A\rangle_1}\right)^2 - \left(\frac{Z}{\langle A\rangle_2}\right)^2\right] \tag{3}$$

Note that α only depends on the symmetry energy term and not on the other terms entering the free

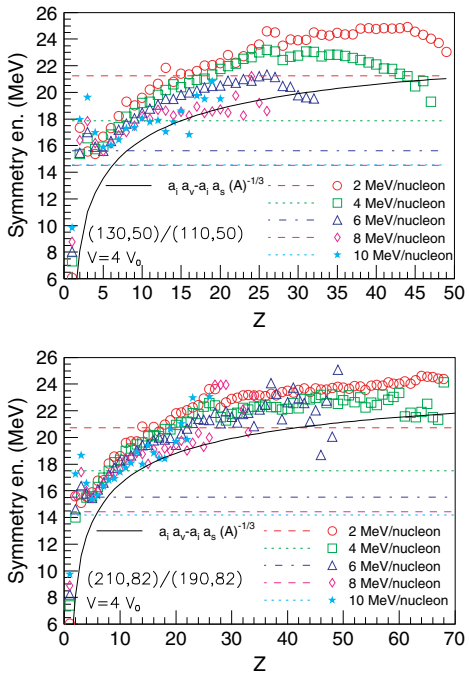

Figure 2: MMM predictions for the symmetry energy as a function of Z at breakup. The atomic mass and charge numbers of the couples of systems are indicated within parentheses. The excitation energies of the sources range from 2 to 10 AMeV. The solid curves indicate the input symmetry energy of the model, dotted and dashed lines the values of C_{sym} according to Eq.4 and symbols those obtained with Eq.3. From [16]

energy. In the formalism, the symmetry energy is that of *hot fragments*. If C_{sym} did not depend on Z, and $(N/Z)_{frag} = (N/Z)_{sys}$, we could get the symmetry energy of the *fragmenting systems*, $S1$ and $S2$:

$$4C_{sym}^{frag}/T = \alpha/\left[\left(\frac{Z_{S1}}{A_{S1}}\right)^2 - \left(\frac{Z_{S2}}{A_{S2}}\right)^2\right]. \tag{4}$$

This approximation was done by several groups [17] who deduced that the values of C_{sym} decrease with the centrality of the reaction, down to values as low as 15 MeV. This implies that the system is at low density. It is however difficult to reconcile these results with the inputs of the statistical model used to derive them (fragments at normal density).

Indeed there is no reason to assume that one can replace in the denominator of Eq.3 the N/Z of fragments by that of the fragmenting sources. This was demonstrated in the framework of the MMM model, as displayed in fig 2. In this figure medium ($A \sim 120$) and heavy ($A \sim 200$) systems are considered. The Z-dependent symmetry energy input in the model, which comprise volume and surface terms, is displayed as full lines. The assumption that Eq.4 is valid leads to Z-independent symmetry energy values (horizontal dashed lines) decreasing when the excitation energy (or temperature) of the sources gets higher. A correct value is in this case only recovered for very heavy fragments at low excitation energy. Conversely the symbols show the symmetry energy calculated with Eq.3. Now the agreement with the input values becomes reasonable for very excited large sources and small fragments, as expected in the grandcanonical framework.

2.3 Isoscaling in dynamical models

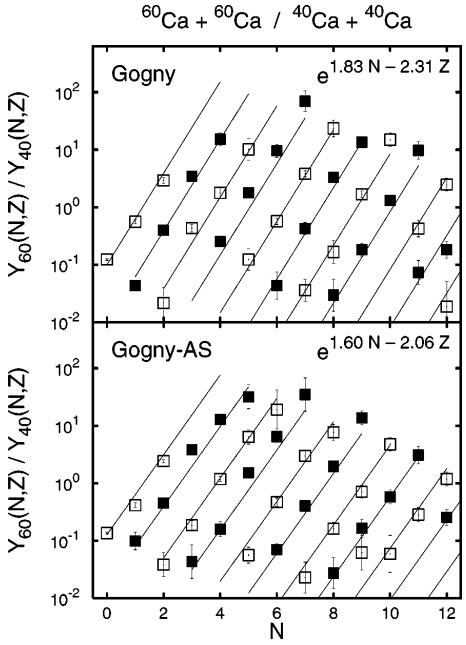

Figure 3: Fragment yield ratios between AMD simulations of central ^{60}Ca+^{60}Ca and ^{40}Ca+^{40}Ca collisions at 35 AMeV at time 300 fm/c. Two different forces, Gogny and Gogny AS were used. From [18]

Somewhat surprisingly, the isoscaling behaviour was also seen for fragments obtained at the end (10^{-21} s) of dynamical simulations [18, 19], as examplified in fig 3. In fact, isoscaling is a general property of fragmenting systems [20]. The relation of the isoscaling parameters to the system properties is more complex in dynamical than in statistical models; they depend on the way fragments are formed and are connected to distillation effects (see sect 7). In short isoscaling does not necessarily require that the system is fully equilibrated. It is observed as soon as the fragment isotopic distributions have Gaussian shapes. The coefficients are determined by the difference between the mean values, divided by the widths of the distributions obtained in the two considered systems [1, 21].

2.4 Effect of secondary decay

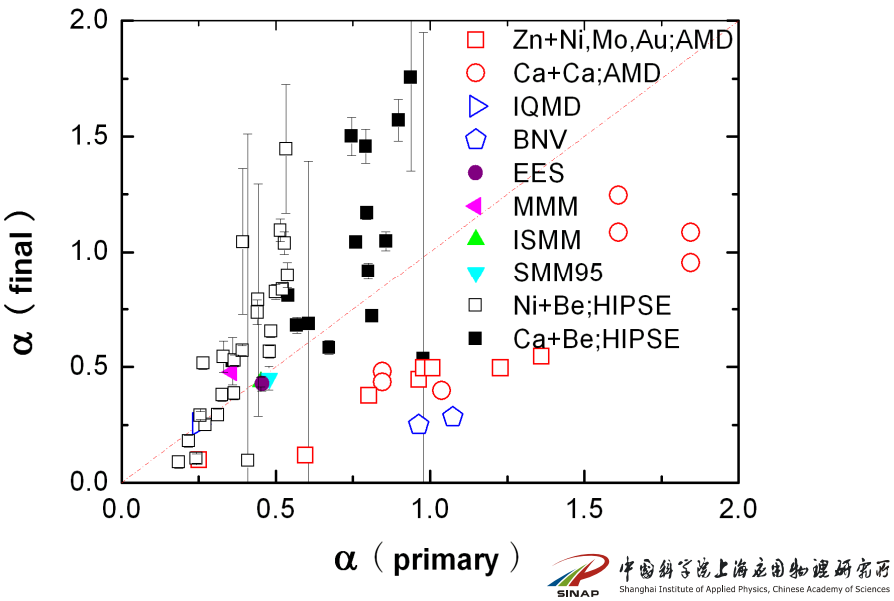

Figure 4: Final vs primary isoscaling α parameters from different models. From [22]

Up to now we have considered the hot fragments present at the freeze-out configuration. However, as mentioned in the introduction, the fragments must be de-excited before comparing their properties to experimental data. The effect of the de-excitation stage on the isoscaling parameters is difficult to evaluate and seems to depend on the models used. Indeed for dynamical simulations (AMD, BNV, IQMD) α is reduced by secondary decay whereas is is moderately affected or increased in statistical models (SMMs, MMM). This is a general trend, as depicted in fig. 4, and in fig.23 of ref [21], where the value of α for final fragments is plotted vs that for primary fragments [21, 22]. A qualitative explanation can be found if one considers α as the ratio between the difference of the mean values of two Gaussian distributions divided by their widths. The primary widths is larger in statistical models. The evaporation process tends to focus the products towards the valley of stability. The difference between the mean values of the distributions for the two systems decreases, and so does the width in statistical models. If the latter effect is more important, α will be increased by the secondary decay. In dynamical models the primary width is narrower, and may be less modified by the secondary decay. The decrease of the shift between the mean values would then dominate and decrease the values of α.

2.5 Isoscaling in the Lattice gas model

The isoscaling properties of fragments were also studied in the framework of a lattice gas model: neutrons and protons occupy a large cubic lattice and interact through nuclear and Coulomb forces. The isotopic distributions of fragments obtained in this picture display isoscaling properties. The value of the α coefficient appears to depend on the fragment charge, as displayed in fig. 5 and more specifically it strongly increases when Z becomes larger than 20. As in section 2.2, one can compare the symmetry energy obtained from the values of α with that input in the model. This is done in fig 6, where the model symmetry energy, plotted vs the temperature (or the density) is depicted by the black line. As previously, using Eq. 4 and the values of α averaged over light (Z=2-7) fragments leads to a constant value of the symmetry energy far from the model one (full green line). Even when taking the more

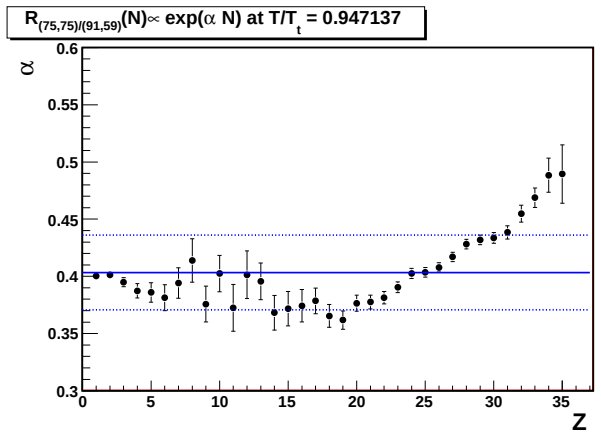

Figure 5: Evolution of the α parameter vs the fragment charge for the systems (N=75,Z=75) and (N=91,Z=59), in the framework of the lattice gas model. From[23].

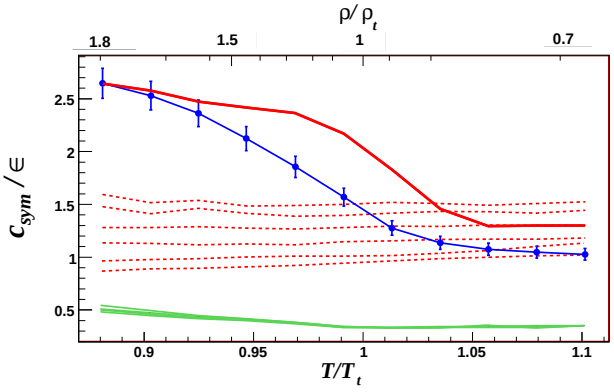

Figure 6: Symmetry energy as a function of the reduced temperature (bottom scale) or the density (upper scale). The black line is the input LGM evolution. Full red line: Eq. 3 applied to the largest fragment. Full green line: Eq. 4 using α averaged over Z=2 to 7. Dotted red lines: Eq. 3 for Z=2 to Z=7. From[23].

correct Eq. 3 but for light fragments, one does not recover the input symmetry energies (dotted red lines). Finally, although not perfect, the symmetry energy obtained from the α values of the heaviest fragments gets closer to the expected value.

This encouraging result underline once more the specific role of the largest fragment of the multifragmentation partitions in determining the thermodynamics of nuclei [24]. It is thus mandatory to measure and identify this fragment in the experiments. Although the most recent 4π arrays (INDRA, CHIMERA) allow to determine its charge and energy, its mass is still out of reach. This is the major aim of the FAZIA project.

2.6 Conclusions on isoscaling and symmetry energy

The isoscaling α parameter extracted for light elements - the only ones isotopically resolved in present experiments - does not appear very reliable for a direct determination of the symmetry energy in the framework of statistical models. More promising is the use of the heavier fragments of the multifragmentation partitions. However these fragments must be detected, as done with the most recent 4π arrays INDRA and CHIMERA, and fully identified. This will be the task of the next generation detectors.

But α is undeniably connected to the symmetry energy, in particular it was shown to linearly vary with the N/Z value of the systems. It appears as a useful isospin dependent variable which can be used to probe dynamical models.

3 the EOS of asymmetric nuclear matter

To a good approximation, at zero temperature, the EOS of asymmetric nuclear matter reads:

$$\frac{E}{A}(\rho, I) = \frac{E}{A}(\rho, I=0) + E_{sym}(\rho) \times I^2 \text{ with } I = \frac{\rho_n - \rho_p}{\rho} = \frac{N-Z}{A}$$ [3]

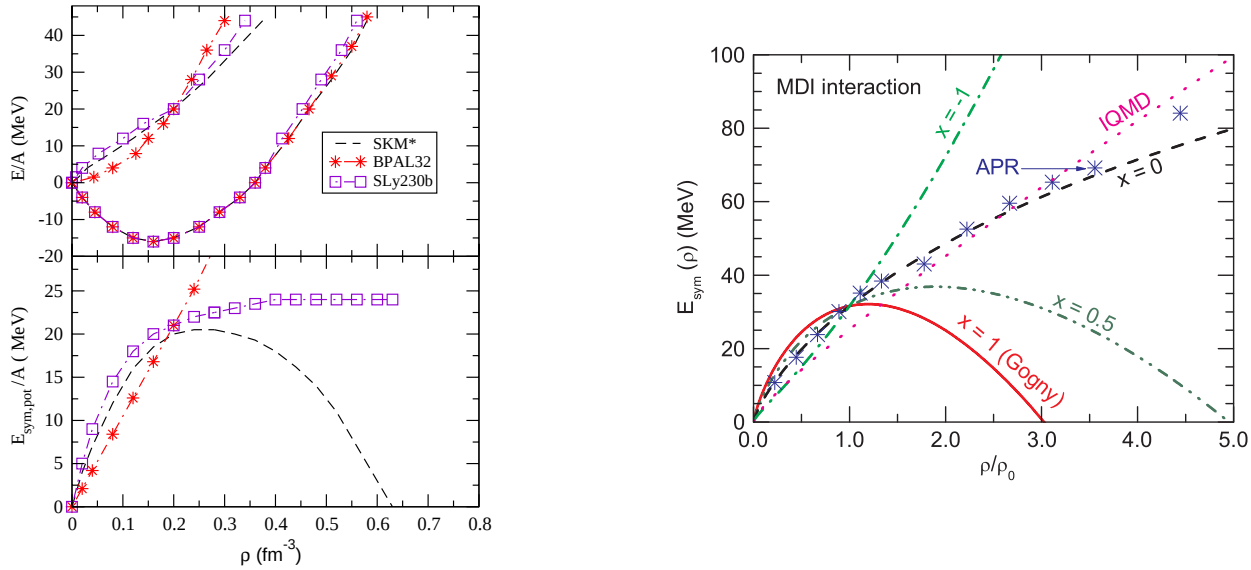

Figure 7: Examples of symmetry energy implementation. Left, from [1] with Skyrme interactions. Right from [2] using momentum dependent interactions.

The first term is the isoscalar term, invariant under proton and neutron exchange, while the second (isovector) one gives the correction brought by neutron/proton asymmetry. For I=1 this terms gives the equation of state of neutron matter. Note that because I is, for most nuclei, smaller than 0.3, the isovector term is much smaller than the symmetric part, which implies that isospin effects should be rather small and all the more difficult to evidence. The availability of Rare Isotopes Beams will, in the future, allow to vary I on a larger range. The present results, detailed in the following sections, were obtained with stable beams.

The symmetry energy, E_{sym}, gets a kinetic contribution, E_{sym}^{kin}, from Pauli correlations and a potential contribution, E_{sym}^{pot}, from the isovector part of the effective nuclear interactions used in models.

$$\frac{E_{sym}}{A}(\rho) = \frac{\varepsilon_F(\rho)}{3} + \frac{C}{2}F(\rho/\rho_0)$$

with $F(1)$=1 and C ≈32 MeV. For convenience in comparing different implementations, examples of which are displayed in fig. 7, E_{sym} is commonly approximated as :

$$\frac{E_{sym}}{A}(\rho) = \frac{C_{s,k}}{2}(\frac{\rho}{\rho_0})^{2/3} + \frac{C_{s,p}}{2}(\frac{\rho}{\rho_0})^{\gamma} \quad (5)$$

or with a second order expansion around normal density :

$$\frac{E_{sym}}{A}(\rho) = E_{sym}(\rho_0) + \frac{L}{3}(\frac{\rho-\rho_0}{\rho_0}) + \frac{K_{sym}}{18}(\frac{\rho-\rho_0}{\rho_0})^2 \quad (6)$$

γ [4], or L define the "asy-stiffness" (terminology proposed by M. di Toro) of the EOS *around normal*

[3] I is also called δ, or β, or η, depending on the papers

γ	Skyrme interactions	MDI
~ 0.2		x=1
~ 0.5	$F3 = \sqrt{\rho/\rho_0}$	
~ 0.7		x=0
1	$F2 = \rho/\rho_0$	
~ 1.4		x=-1
~ 1.6	$F1 = \frac{(\rho/\rho_0)^2}{1+\rho/\rho_0}$	

Table 1: Values of the γ exponent obtained by adjusting, on a density range 0.7-1 ρ_0, a power law on the functionals used for the potential term of the symmetry energy, either given by $F1$, $F2$, $F3$, or as a function of x in [25, 26].

density. The symmetry energy is said "asy-soft" if E_{sym}^{pot} presents a maximum (between ρ_0 and $2\rho_0$), followed by a decrease and vanishing (γ <1) [5] and "asy-stiff" if it continuously increases with ρ ($\gamma \geq 1$). The values of γ associated to some Skyrme interactions with functionals $F1$, $F2$, $F3$ [27], or to momentum-dependent interactions characterized by a variable x [25, 26] are given in Table 1. In this latter case, the functional with x=1 corresponds to the original Gogny force.

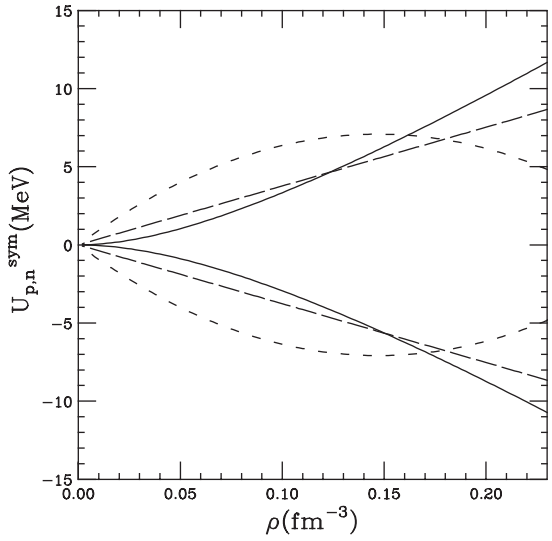

Figure 8: Symmetry contribution to the mean field, for I=0.2, for neutrons (upper curves) and protons (lower curves). Dashed lines for asy-soft ($\gamma \sim 0.5$), long dashed lines for asy-stiff ($\gamma = 1$) and solid lines for asy-superstiff ($\gamma \sim 1.6$). From [1].

Isospin effects in nuclear reactions can be connected to the opposite signs of the neutron and proton potentials, as shown in fig. 8 for a nucleus with I=0.2, e.g. ^{124}Sn. The symmetry potential is repulsive ($U > 0$) for neutrons. At subsaturation densities ($\rho \lesssim 0.16$) it is more repulsive in the asy-soft case, whereas above normal density the repulsive character increases with the asy-stiffness. Conversely the symmetry potential is attractive for protons, which means that *it acts in opposition with the Coulomb potential.*

[4] Warning: in some papers, particularly those of Bao-An Li, the γ is used to characterize the total symmetry energy, including the kinetic term.

[5] Rigourously a function with a maximum, as the ones with $x > 0$ in fig. 7 can not be fitted with a power law having a positive exponent, which are continuously increasing functions. Indeed, as the development (Eq. 6), Eq. 5 is considered around normal density and γ is determined from a fit of the used functional on a density range slightly below ρ_0.

3.1 Transport codes

The dynamical approaches used to simulate heavy-ion collisions at energies of some tens to hundreds of MeV per nucleon can be classified in several types. The first ones solve Boltzmann-like kinetic equations for the one-body distribution in phase space, in the limit $hbar \rightarrow 0$.

$$\frac{\partial f(\mathbf{r},\mathbf{p},t)}{\partial t} + \frac{\mathbf{p}}{m}.\nabla \mathbf{r} f(\mathbf{r},\mathbf{p},t) - \nabla \mathbf{r}\mathcal{U}(\mathbf{r},t).\nabla \mathbf{p} f(\mathbf{r},\mathbf{p},t) = I_{coll}^{UU}(f)$$

Stochastic extensions of these equations, developed in order to recover fluctuations allowing the formation of fragments, form a second class: a Langevin term δI is added to account for the fluctuating part of the collision term. Exact solutions of the Boltzmann-Langevin equation being difficult to obtain, the fluctuating collision term can be approximated by a fluctuating Brownian force, with a null average value, as done in BOB, or SMF simulations The third class are the molecular dynamics models, which study the motion of all the particles of a system under their mutual interactions. More quantal approaches make use of Gaussian wave packets to represent the A particles. The codes which are quoted in the following sections are summarized in table 2, in appendix A. A critical description of each class of transport codes can be found in [28].

Concerning the ingredients of these codes, the isoscalar term of the nuclear interaction, following the results of the last two decades, is chosen soft, with an incompressibility parameter K_∞=200-230 MeV. This value is compatible with the measurements of the energy of the isoscalar monopole resonance in nuclei [29]. A momentum dependence appears in some implementations, sometimes in the isoscalar part only and sometimes also in the isovector component.

In the first class of models, the mean field is complemented by the residual interactions, which gives the semi-classical version of the nuclear Boltzmann equation. The collision term $I_{coll}^{UU}(f)$ depends on a collision rate containing a differential nucleon-nucleon cross-section. Note that, although the nucleon-nucleon interaction is splitted between mean field and residual interaction, it is a *single* interaction. This means that the cross section in the collision term should not be chosen independently of the mean field but evaluated from imaginary part the Brückner G-matrix, the real part of which being the mean field. Practically however both terms are not consistently calculated, and the residual interaction is implemented either with the free $\sigma_{NN}(E,I,\theta)$ or with some recipe for in-medium correction. Note also that, somewhat surprisingly, a collision term is added in some molecular dynamics codes (QMD), although in principle the complete A-body problem is treated in such models.

Finally, except FMD and AMD, all these transport codes are semi-classical in nature. The Fermionic nature of the system gets lost with time[6]. A consequence is that these codes are "reliable" on a short range of time, and thus can not treat the secondary decay. Hot fragments must therefore firstly be recognized:

- using a clusterization algorithm, in r space or in r,p space e.g. MST or ECRA in MD codes.
- following local densities : low densities correspond to free nucleons, higher ones to clusters of nucleons (fragments)[7].

and then input with their characteristics in a statistical code in order to de-excite them.

[6] The CoMD code however constrains occupation numbers to remain strictly lower than 1, which makes the system Fermionic all over the collision time

[7] The mean field codes can lead to the formation of fragments, either through a stochastic implementation, or taking advantage of numerical fluctuations. They can not however recognize light particles (H, He isotopes)

The comparisons between experimental data and models presented in the next sections were made in such a way that *the properties of symmetric matter and the residual interaction were fixed, whereas the form of E_{sym} was varied.*

3.2 Nuclear collisions around and above the Fermi energy

Collisions are classified through their violence, which reflects the impact parameter. One generally roughly distinguishes central (∼head-on) and (semi)-peripheral collisions.

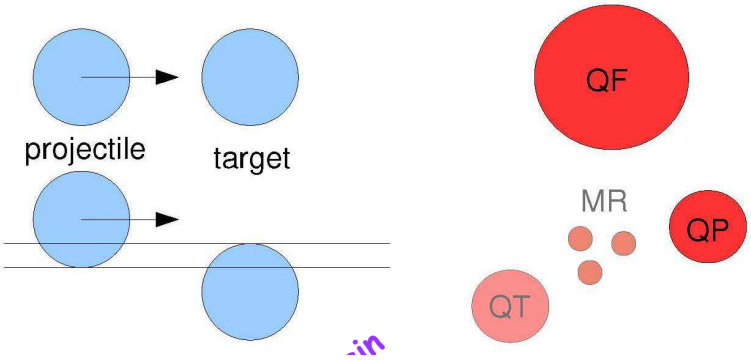

Around and above the Fermi energy almost all collisions end-up with two big nuclei, remnants of projectile (QP) and target (QT). A fraction of the collisions also present a copious (fast) emission of nucleons and light fragments with velocities intermediate between those of the QP and QT. This is termed mid-velocity or neck emission. In central collisions topology selectors allow to isolate reactions in which a big remnant is formed which, depending on its energy either de-excite to an evaporation residue, or multifragments.

Most of the data presented in the following have been acquired with the help of large charged products arrays (see appendix B for a glossary).

4 Competition of reaction mechanisms

Isospin is expected to govern the competition between fusion and deep inelastic reactions in semi-central collisions ($b \sim 0.4 b_{max}$, b_{max} being the grazing impact parameter), at energies slightly below the Fermi energy. The effect of isospin can be understood in terms of the amount of attraction or repulsion existing during the approach phase of the two nuclei. During this phase, for a density slightly above ρ_0, the symmetry energy is larger in the asy-stiff case. For neutron-rich systems, fusion is favoured with an asy-soft EOS: neutrons are dominant, and their effect is less repulsive in that case. For neutron-poor systems, conversely, fusion is easier for an asy-stiff EOS, because the dominant protons have a larger attractive symmetry potential. (see the evolution of collisions at 30 A MeV between ^{46}Ar and ^{64}Ni, and ^{46}V and ^{64}Ge for b=4 fm in fig.5-1 of ref. [1].)

The isospin effect on the reaction dynamics was experimentally studied in ref. [30]. Targets of ^{40}Ca, ^{46}Ti, and ^{48}Ca were bombarded by a ^{40}Ca beam accelerated at 25 A MeV. Charged reaction products were detected with the CHIMERA 4π array. The competition between fusion and deep inelastic reactions in central collisions was explored through the study of the variable $\Delta M_{nor} = (M_1 - M_2)/M_{tot}$, M_1, M_2 being the masses of the largest and second largest detected fragment and M_{tot} the total mass of the

incident system [8]. Indeed a fusion reaction, ending with a heavy residue and evaporated light charged particles will be associated to large values of ΔM_{nor}. Conversely deep inelastic reactions for these almost symmetric systems, should have ΔM_{nor} values closer to zero. ΔM_{nor} minimizes the effects due to the mass differences between the targets and enhances those coming from their isotopic content. The

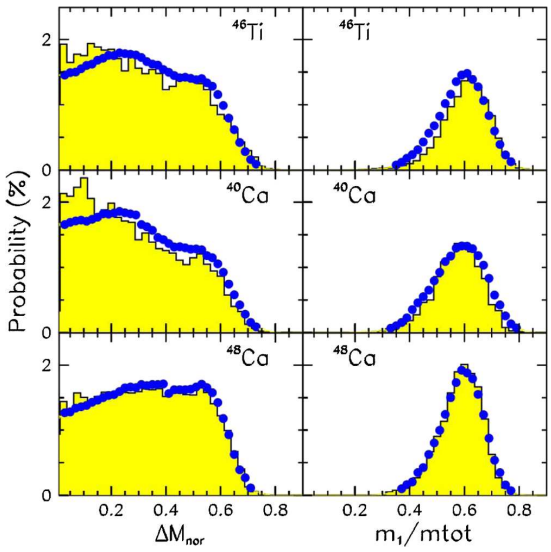

Figure 9: Probabilities of ΔM_{nor} (left) and of the normalized mass of the largest fragment (right) for the 3 studied systems. Blue dots represent experimental data whereas the shaded histograms show the results of a CoMD+GEMINI calculation. From[30].

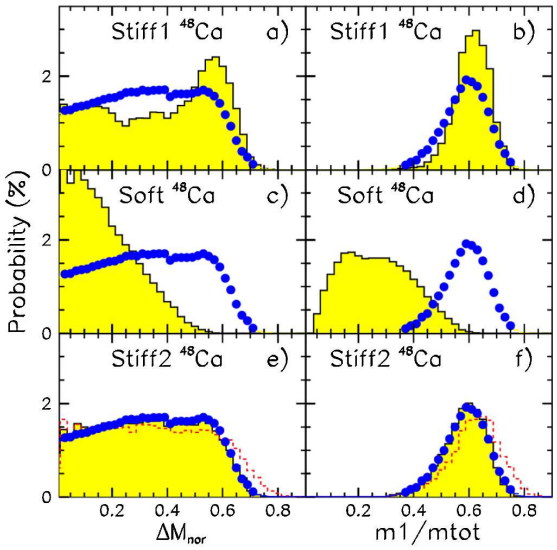

Figure 10: Same as fig. 9 for the ^{40}Ca+^{48}Ca. CoMD+GEMINI calculations with different parametrizations are shown. Top panels: stiff1, medium panels: soft and bottom panels: stiff2. The dashed lines show the results of CoMD without the GEMINI secondary decay step. From[30].

results are displayed in fig. 9. The distributions of ΔM_{nor} clearly show that there are more fusion events (characterized by ΔM_{nor} larger than 0.4) for the heavy ^{48}Ca target than for the two others. Indeed, due to the neutron richness of ^{48}Ca the compound nucleus is close to the valley of stability while the other ones lie near the proton-drip line. Information on symmetry energy was extracted by comparing experimental findings to the results of constrained molecular dynamics (CoMD) simulations [31]. The symmetry energy is implemented with three different stiffness, labelled stiff1, stiff2 and soft on fig. 9 and 10 [9]. All impact parameters up to b_{max} were included in the simulations and the same selections as in the experiment were imposed to the calculated events. The results are shown as histograms in fig. 10 for the ^{40}Ca+^{48}Ca system. The shape of the ΔM_{nor} distribution is clearly very dependent on the asy-EOS: for the stiffer case (stiff1) there is too much fusion, whereas in the soft case the system almost completely disintegrates due to the strongly repulsive interaction. A good matching with the experiment is obtained in the stiff2 case, for the three systems, namely for a potential symmetry term linearly increasing with density (γ=1$\pm$0.15). Note that in this case the effect of secondary decay is weak

[8] For the pertinence of the analysis, complete events ($\sum_i Z_i$ >80% Z_{tot} and $\sum_i P_i > 0.7 \times P_{beam}$) were selected, and a velocity gate was set to eliminate quasi-targets).

[9] stiff1≡F1; stiff2≡F2; soft≡F3 - see table 1.

(compare the dashed lines and the shaded histograms in fig. 10).

5 Isospin diffusion

5.1 Theoretical frame

Isospin diffusion is related to isospin exchange between the projectile- and target-like fragments during a semi-peripheral nuclear collision. Ultimately if the reaction time is long enough the system can reach isospin equilibrium, both partners ending with the total system isospin [10]. Isospin diffusion arises from two phenomena:

1. Isospin transport due to density gradients (migration), which depends on the slope of the symmetry energy :

$$D_{\rm n}^{\rho} - D_{\rm p}^{\rho} \propto 4I\frac{\partial E_{sym}}{\partial \rho}$$

2. Transport due to isospin concentration gradients (diffusion), which depends on the absolute value of the symmetry energy

$$D_{\rm n}^{I} - D_{\rm p}^{I} \propto 4E_{sym}$$

In the hope of minimizing effects such as pre-equilibrium emission, Coulomb, secondary decay ..., and of emphasizing those due to isospin, it was proposed to use a ratio, providing the same measurement is performed for several systems differing only by their isospin content. One chooses an isospin sensitive quantity x and constructs the imbalance, or isospin transport, ratio, R^x, defined as:

$$R^x_{P,T} = \frac{2(x^M - x^{eq})}{(x^H - x^L)} \text{ with } x^{eq} = (x^H + x^L)/2$$

H and L refer to two symmetric reactions between n-rich and n-poor nuclei, M to the mixed reaction. By construction $R = \pm 1$ in projectile(P)/target(T) regions, and R=0 when isospin equilibrium is reached. Different observables x will provide the same result if they are linearly related. Such a ratio, where $x = (N-Z)/(N+Z)$, the true isospin content of the QP and QT, was calculated in SMF simulations. The considered systems are Sn+Sn, with H=124 and L=112, at two energies 35 and 50 AMeV. The simulations were performed for different impact parameters and the results are plotted versus the normalized dissipated energy, $E_{loss}/E_{c.m.}$. It is interesting to observe in fig. 11 that such a representation leads to a "universal" curve [32], which depends neither on the incident energy nor on the isoscalar interaction used in the simulation [11], but only on the symmetry energy parametrisation (soft, γ=0.5 and stiff γ=1). The main information visible on this figure is that isospin equilibrium is reached faster, and for less dissipative collisions in the asy-soft case.

[10] The reaction time runs from the contact between projectile and target up to the instant at which QP and QT reseparate. It thus depends on the incident energy and on the impact parameter.

[11] Two soft isoscalar interactions are used, with (MD) or without (DI) momentum dependence. Note that the momentum dependence, when adopted, acts also on the isovector part of the EOS and modifies its strength. The free σ_{NN} with its isospin energy and angular dependence is taken.

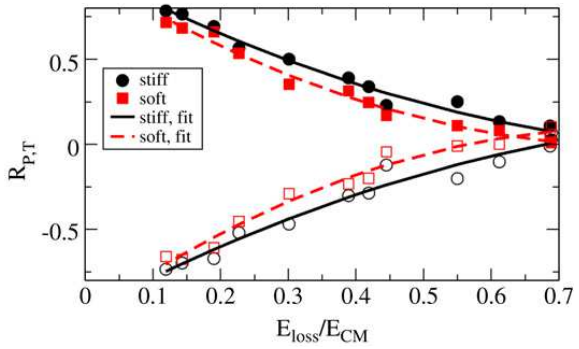

Figure 11: Imbalance ratio as a function of the relative energy loss for Sn+Sn reactions at 35 and 50 A MeV. The points are calculated for asy-soft and asy-stiff MD or MI interactions and the lines are quadratic fits to all points. From[32].

5.2 Experimental studies: one impact parameter

Isospin diffusion has been deeply studied by the MSU group since 2004. They look at four reactions, ^{124}Sn+^{124}Sn, ^{112}Sn+^{112}Sn, ^{124}Sn+^{112}Sn and ^{112}Sn+^{124}Sn at 50 A MeV. Two isospin variables were considered, the isoscaling parameter ($x = \alpha$) and the ratio of yields of mirror nuclei ($x = \ln\left[Y(^7Li)/Y(^7Be)\right]$). Both are linearly connected with I. An experimental impact parameter is obtained from the measured charged product multiplicity, M_{cp}, distributions and peripheral collisions are considered: b/b_{max}>0.8. Along the years the experimental results were confronted with those of several dynamical simulations, with the condition: b=6 fm, and $x = I$. The first comparison was performed with

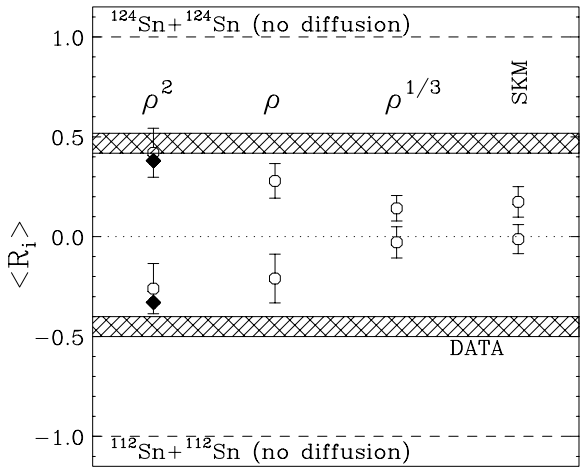

Figure 12: Measured (shaded bars) and calculated (points) values for R^α. The labels on the calculated values represent the density dependence of E_{sym}^{pot}, which gets softer from left to right. From [33].

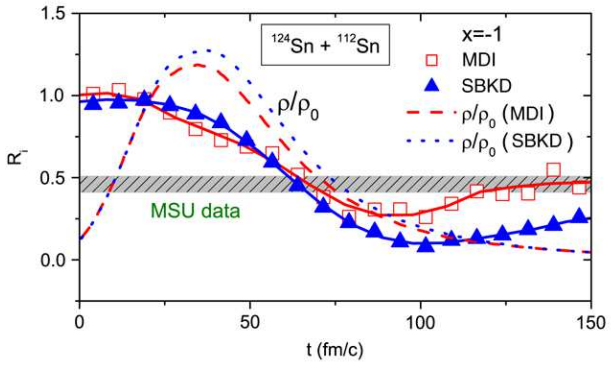

Figure 13: The degree of isospin diffusion as a function of time (points and full lines) with the MDI and SBKD interactions. The corresponding evolutions of central density are also shown as dashed/dotted lines. From[26].

the BUU97 [34] and is shown in fig. 12. Four parameterizations of E_{sym}^{pot}, indicated on the figure, were used. For the considered peripheral collisions, the asymptotic value of R^I is reached at ∼100 fm/c [12]. The filled points show that in that case the secondary decay has a weak influence on R^I, as they remain

[12] 300 fm/c = 10^{-21} s.

close to the corresponding open points, calculated at 260 fm/c. The shaded horizontal bars indicate the experimental values obtained for R^{α}. It is clear that the best agreement is obtained for a stiff asy-EOS, depending almost quadratically on the density (γ ~1.5-2). Note that the value of R is around 0.5, indicating that isospin equilibration is not obtained for these systems in peripheral collisions. Later the data were compared with the results of calculations with a momentum dependent (MDI/IBUU04) and independent (SBKD) interactions. The density dependence of the symmetry energy is the same in both cases. It is instructive to observe in fig. 13 that isospin diffusion essentially occurs during the expansion phase of the collision, at subnormal density. Here again a good agreement between the asymptotic calculated value and the data is obtained for the MDI, which is asy-stiff (x =-1 $\equiv$ γ= 1.4). Finally more recently the MSU group compared their data with an improved molecular dynamics code (ImQMD [35]). In that case they used the two variables R^{α} and R^{7}, as displayed in fig 14. It may first be noticed that both experimental values are in good agreement (R^{7} must be considered in the projectile rapidity region y/y_{beam} >0.8). The best reproduction of these data with ImQMD is obtained for an asy-soft EOS ($0.45 \leq \gamma \leq 1$).

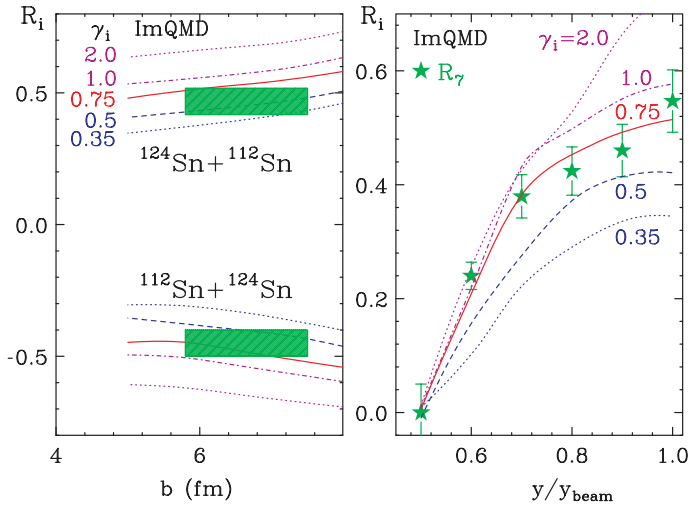

Figure 14: Left panel: comparison of R_{α} (shaded regions) to ImQMD results (lines) as a function of the impact parameter for different values of γ. Right panel:comparison of R_7 from the yield of mirror nuclei (A=7, stars) as a function of the rapidity to ImQMD calculations at b=6fm. From [36].

5.3 Experimental studies: towards isospin equilibration

The INDRA collaboration performed investigations on isospin transport effects on the reaction dynamics for two systems, with the same projectile, ^{58}Ni, and two different targets,^{58}Ni and ^{197}Au, at incident energies of 52A MeV and 74A MeV [37, 38]. The evolution of isospin effects in different conditions of charge (and mass) asymmetry was followed as a function of the energy deposited into the system:
$E_{diss} = E_{c.m.} - \frac{1}{2}\mu V_{rel}^2$ with $V_{rel} = V_{QP}^{rec} \times \frac{A_{tot}}{A_{target}}$
The data were compared to the results of BNV simulations [13], with two different parameterizations for the potential symmetry term: an asy-stiff EOS, that has a linear density dependence, and an asy-soft one using the SKM* parameterization corresponding roughly to γ ~0.6. The BNV simulations show that the chosen sorting variable gives a good measure of the impact parameter, as shown in fig. 15. The

[13] A soft isoscalar EOS, K_{∞} = 200 MeV and the free nucleon-nucleon cross section, with its energy, isospin and angular dependence are used.

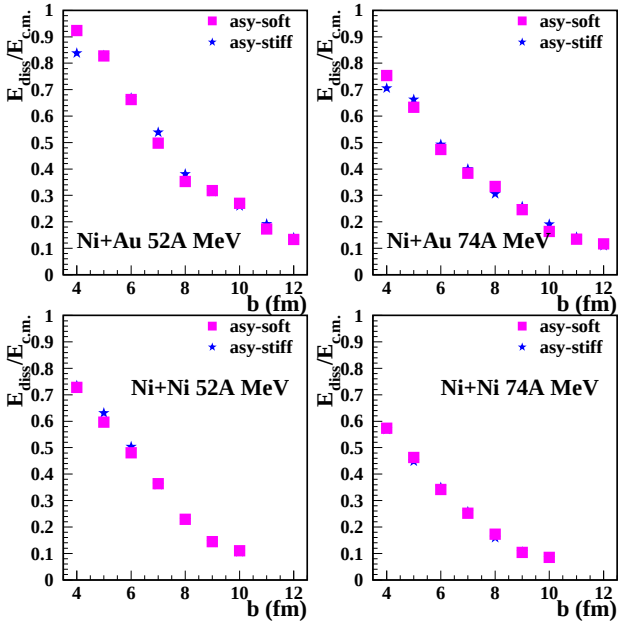

Figure 15: Correlation between $E_{diss}/E_{c.m.}$ and the impact parameter in BNV simulations, with different symmetry energy terms. From [38].

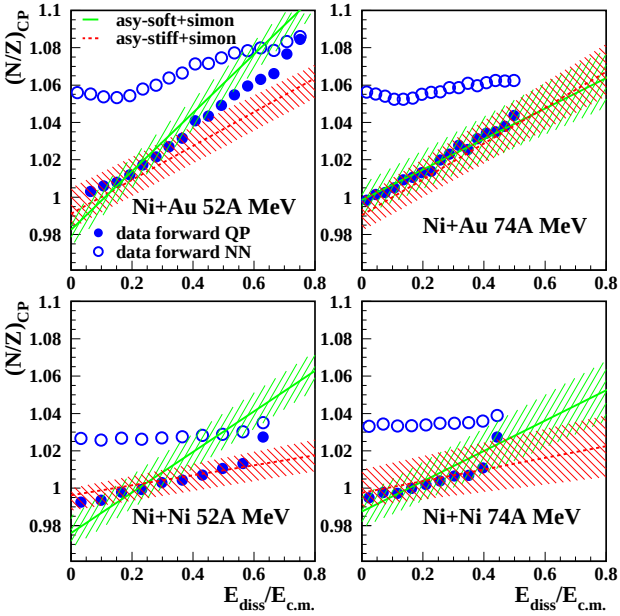

Figure 16: Isospin ratio of complex particles for Ni quasi-projectiles vs $E_{diss}/E_{c.m.}$. Open circles correspond to experimental data forward of the N-N velocity, close circles to those forward in the QP frame. Lines and hatched zones correspond to the results of simulations after de-excitation of the QPs. From[38].

isospin-dependent variable was constructed from the isotopically identified particles included in the QP:

$$(< \mathrm{N} > / < \mathrm{Z} >)_{\mathrm{CP}} = \sum_{N_{evts}} \sum_{\nu} N_\nu / \sum_{N_{evts}} \sum_{\nu} P_\nu \qquad (7)$$

where N_ν and P_ν are respectively the numbers of neutrons and protons bound in particle ν[14]; free protons are excluded, as free neutrons are not measured. N_{evts} is the number of events contained in the dissipated energy bin considered. The variable $(\mathrm{N/Z})_{\mathrm{CP}}$ was calculated twice: first considering particles forward emitted in the nucleon-nucleon frame ($\mathrm{V_{particle}} > \mathrm{V^{lab}_{proj}}/2$), and secondly keeping only particles forward emitted in the QP frame ($\mathrm{V_{particle}} > \mathrm{V^{rec}_{QP}}$). Indeed as the BNV simulation does not allow to identify mid-rapidity particles and light fragments, the theoretical value of $(\mathrm{N/Z})_{\mathrm{CP}}$ is calculated only from the particles evaporated by the QP, which are experimentally approximated as the particles forward emitted in the QP frame.

The results are displayed in fig 16. The lines represent the theoretical evolution of $(\mathrm{N/Z})_{\mathrm{CP}}$, obtained after de-exciting the hot QP obtained in the simulations at the instant of re-separation QP-QT with the SIMON code. For the Ni+Ni system the variation of $(\mathrm{N/Z})_{\mathrm{CP}}$ with centrality is small, and attributed to pre-equilibrium emission. At both energies $(\mathrm{N/Z})_{\mathrm{CP}}$ grows slightly higher at high dissipation for the asy-soft case. For this system it must be noted that secondary decay modifies the trends observed

[14] ν being d, t, ^{3}He, ^{4}He, ^{6}He, ^{6}Li, ^{7}Li, ^{8}Li, ^{9}Li, ^{7}Be, ^{9}Be, ^{10}Be.

for the hot QP [38]. The evolution with centrality is much more pronounced for the neutron-rich and asymmetric Ni+Au system. In addition to pre-equilibrium effects, isospin transport takes place between the two partners of the collision, and increases with the violence of the collision. $(N/Z)_{CP}$ is higher in the asy-soft than in the asy-stiff case at 52 A MeV, while it appears quite independent of the asy-stiffness at 74 A MeV. For this system the evolution of $(N/Z)_{CP}$ with $E_{diss}/E_{c.m.}$ is strongly attenuated with respect to that of the hot QPs, but the order asy-soft/asy-stiff is not modified.
The open points show the experimental values obtained forward in the NN frame. Let us remind that in this case mid-rapidity particles are mixed with those coming from the QP de-excitation. For the Ni+Ni system at both incident energies, $(N/Z)_{CP}$ varies by at most 1.5% when dissipation increases. This is the expected behaviour for this symmetric system where N/Z is only modified by pre-equilibrium emission. For the Ni+Au system the isospin ratio is higher than that of the Ni+Ni system whatever the dissipated energy and presents a significant increase with dissipation. The maximum value reached is higher at $52A$ MeV, while the trend is flatter at $74A$ MeV. This may be interpreted as a progressive isospin diffusion when collisions become more central, in connection with a larger overlap of the reaction partners and thus a longer interaction time. For a given centrality, the separation time is longer at $52A$ MeV than at $74A$ MeV, leaving more time to the two main partners to go towards isospin equilibration.
The close points in fig 16 are related to the values of $(N/Z)_{CP}$ forward in the QP frame. They are in all cases smaller than the previous ones, and for Ni+Au at both energies, they grow faster with dissipation. This is because the mid-rapidity particles are no longer included: it is known that these particles are more neutron-rich, and that their isospin content is independent of the violence of the collision [39].

The values of $(N/Z)_{CP}$ forward in the QP frame can be compared with the results of the simulations. A first result worth mentioning is that the chemical composition (N/Z) of the quasi-projectile forward emission appears as a very good representation of the composition of the entire quasi-projectile source. Such an observation seems to validate a posteriori the selection frequently used to characterize the QP de-excitation properties. When looking *globally* at the results for the four cases treated here, the agreement is better when the asy-stiff EOS is used, i.e. a linear increase of the potential term of the symmetry energy around normal density. Note however that for Ni+Au at 52 A MeV, where isospin transport effects are dominant, the close points lie in between the simulated results with the two EOS. This observation allows us to put an error bar on our result, expressed as $\gamma=1\pm0.2$.

This experiment also gives information on the equilibration of isospin. Firstly it can be derived directly from the experimental data. In the top-left panel of fig 16 one observes that the open and close points superimpose at high dissipation: it means that the values of $(N/Z)_{CP}$ are the same at mid-rapidity and at velocities close to that of the QP. This is a strong indication of isospin equilibration. Note that more than 75% of the energy must have been dissipated before equilibrium is reached. Qualitatively this high value of the dissipated energy at isospin equilibration pleads for an asy-stiff EOS (see fig 11). On the theoretical side, equilibration is reached in simulations for an impact parameter $b \lesssim 4$ fm, at a time t=130±10 fm/c.

6 n/p ratio at Fermi energies

The ratio of the yields of emission of neutrons and protons is directly sensitive to the symmetry energy, due to the opposite signs of the neutron and proton symmetry potentials. The most important information comes from high energy nucleons, because they are early emitted.

This variable was experimentally studied by the MSU group [35, 36, 40]: they measured center-of-mass proton and neutron energy spectra for $70° < \theta_{cm} < 110°$, in central collisions. Protons and light

clusters were identified with LASSA modules, neutrons were detected in a neutron wall. Part of the WU Microball served as an impact parameter selector. Neutrons and protons contained in light clusters, not taken into account in a first analysis were included in the late ones. To minimize uncertainties due to the different apparatuses, calibrations, efficiencies for neutron and proton measurements, they performed two experiments at 50 AMeV on a neutron-poor system ^{112}Sn+^{112}Sn (L) and a neutron-rich one ^{124}Sn+^{124}Sn (H) and use double ratios of spectra:

$$DR(n/p) = R_{n/p}(H)/R_{n/p}(L)$$

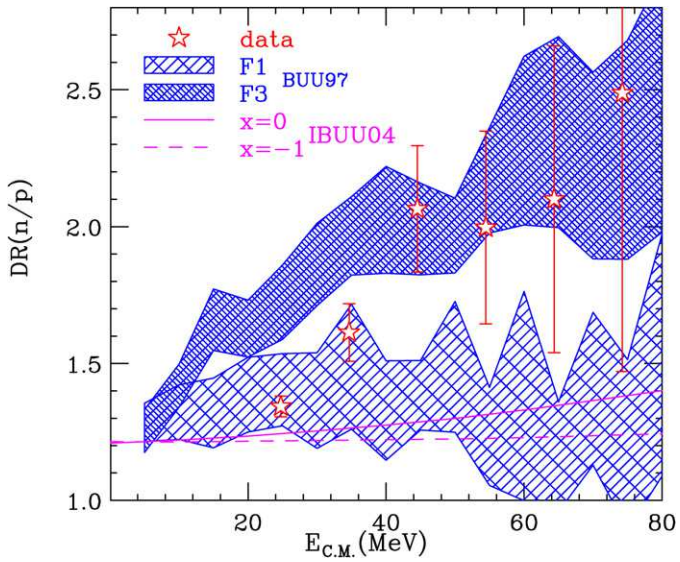

Figure 17: Coalescence invariant neutron-proton double ratios plotted as a function of kinetic energy of the nucleons. The shaded regions represent calculations from the BUU97 simulations from [41]. The solid and dashed lines represent the results of IBUU04 calculations at b=2 fm from [42]. The experimental data of [40] are displayed by stars. From [35].

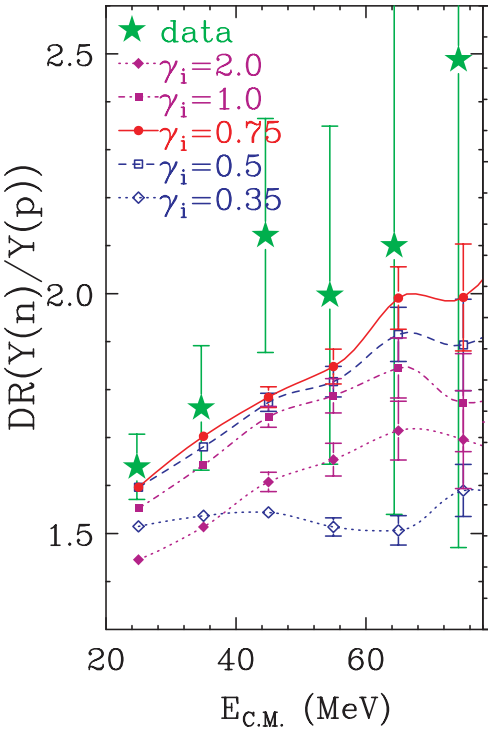

Figure 18: Comparison of experimental double neutron-proton ratios [40] (stars) as a function of nucleon center-of-mass energy, to ImQMD calculations (lines) with different density dependencies of the symmetry energy. Adapted from [36].

The experimental data were compared with the results of the same transport codes used for isospin diffusion (section 5.2), varying the symmetry energy term. The BUU97 (fig. 17, hatched zones - see sect. 3 for the meaning of $F1$ and $F3$) best matches data for a soft asy-EOS (γ=0.5), whereas the IBUU04 model, with a momentum dependent interaction, (lines) completely fails in reproducing the data. It is known that preequilibrium emission is strongly increased when using momentum dependent interactions [43], but the isospin content of this emission may also be modified. A more detailed comparison, shown in fig 18 was performed with the ImQMD code. It is interesting to observe that the calculated double ratio presents maximum values for a symmetry energy such as γ=0.75. Increasing or decreasing γ diminishes the calculated double n/p ratio. The experimental data lie above the maximum calculated values, but

have large error bars. The authors of [36] state that, within a 2σ uncertainty, the potential symmetry energy should have a density dependence such as $0.5 \leq \gamma \leq 1.05$, with best value 0.7.

These authors stressed that the ImQMD code privilege the same form of E_{sym} when confronted to isospin diffusion and n/p ratio experimental data, which strengthens that result. Conversely the BUU97 and IBUU04 do not lead to consistent results for these two variables. Particularly, with the momentum-dependent interaction of IBUU04 the increase of preequilibrium emission, which occurs in the same time interval as isospin diffusion, should modify the respective influence of these two phenomena.

7 Isospin distillation (or fractionation)

Isospin distillation is a phenomenon expected to occur in central collisions followed by multifragmentation. It is a test of symmetry energy in dilute matter and a signature of a liquid-gas type phase transition. The origin of this phenomenon is easily understood when looking at the evolution of the neutron and proton chemical potentials [15] with density, as displayed in fig 19. The differences of the local chemical potentials, for neutrons and protons, which can be expressed as $\mu_n - \mu_p = 4E_{sym}(\rho)I/A$, governs the mass flow in non equilibrium systems. In the density region reached by multifragmenting

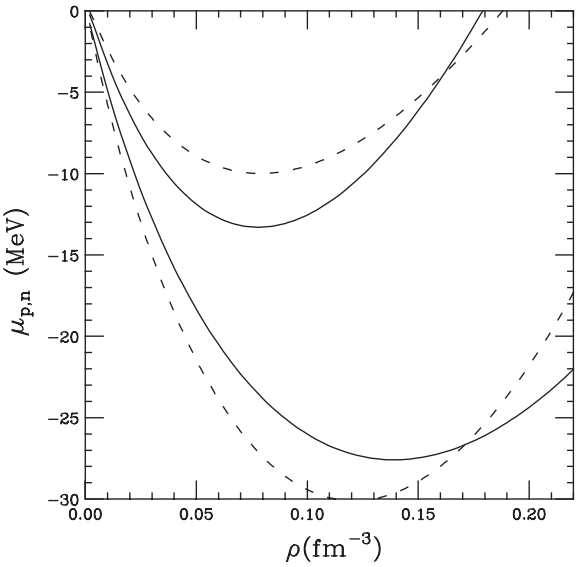

Figure 19: Density dependence, for I=0.2, of neutron (upper curves) and proton (lower curves) chemical potentials for asy-superstiff ($\gamma \sim$1.6 - solid lines) and asy-soft (γ=0.5 - dashed lines) EOS. From [1].

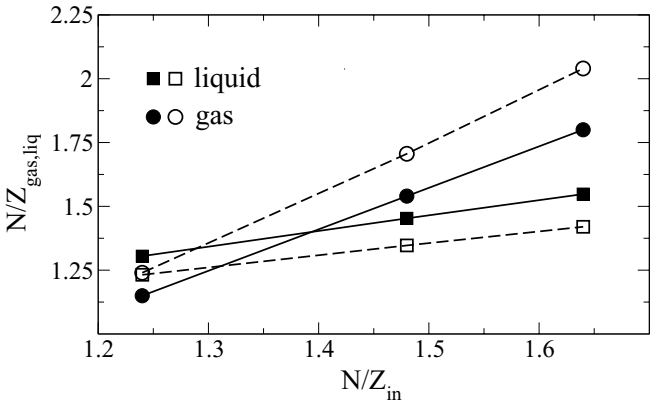

Figure 20: The asymmetry N/Z of the gas (circles) and of the liquid (squares) phase for central Sn+Sn collisions with different initial N/Z. Solid lines and solid symbols refer to the asystiff parametrization, and dashed lines abd open symbols refer to the asy-soft parametrization. From [44].

systems ($\rho \lesssim \rho_0/2$, i.e. $\rho \lesssim$0.08 on the figure) one can observe that neutrons and protons move in phase, both towards higher ρ. The slope of μ_p is however steeper than that of μ_n. This means that the

[15] We remind that the chemical potential is the derivative of the energy with respect to the number of particles of the system.

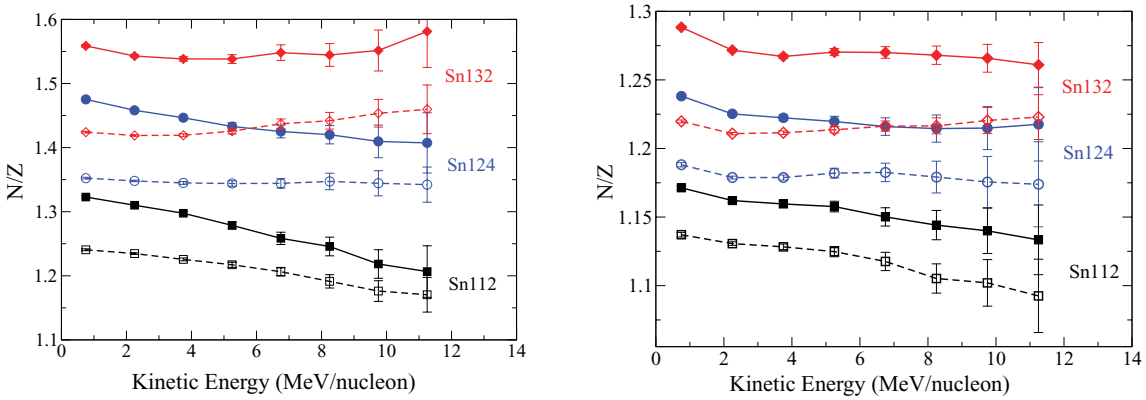

Figure 21: The fragment asymmetry N/Z as a function of the kinetic energy for different symmetric Sn+Sn collisions at b=2 fm, E/A=50 AMeV, obtained with an asy-stiff (solid lines) and asy-soft (dashed lines) EOS. Left panel: hot primary fragments; right panel final cold fragments. From [44].

clusters (high density) produced by bulk instability will be more symmetric while the gas phase (low density) will get enriched in neutrons. As the difference between the chemical potential slopes is more marked for an asy-soft EOS (dashed lines), the distillation effect will be stronger in that case. Dynamical simulations with the BNV code were performed for central (b =2 fm) symmetric Sn+Sn collisions, with masses 112, 124 and 132, at 50 AMeV [44]. A large statistics is necessary to observe isospin effects, which are looked for by using two forms of E^{pot}_{sym} in the interaction, a stiff one corresponding to $\gamma \sim$1.6 and a very soft one ($\gamma \sim$0.2-0.3). The isospin content of the liquid (fragment [16]) and gas phases are depicted as a function of the initial N/Z in fig. 20. The fragments here are the primary hot ones. It appears that the N/Z of the gas phase is larger than that of the liquid; the difference increases with the initial N/Z, and is larger in the asy-soft case because the symmetry energy at low density is larger. For the less neutron-rich system, the liquid phase is more neutron-rich than the gas in the asy-stiff case; this inversion is caused by Coulomb effects which become dominant over symmetry effects, leading to a strong proton emission. Finally one can notice that $I_{frag} < I_{syst}$ for n-rich systems and conversely $I_{frag} > I_{syst}$ for "n-poor" systems.

Experimentally it is difficult to define a limit in Z between the liquid and gas phases, it may vary from event to event. The symmetry energy effect can however be traced back by analysing in the same way the evolution of the N/Z [17] of the fragments as a function of their kinetic energy, in experiments and simulations (i.e. without caring whether fragments come the liquid or in the gas phase). This is shown in fig. 21 which displays the results obtained in the simulations. On the left panel, which concerns hot fragments, it appears that the magnitude, but also the slope of the fragment asymmetry vs E depends on the symmetry energy. The slope appears as the final result of two opposite trends: the Coulomb accelerate the more proton-rich fragments, which would give a negative slope. The symmetry energy is more repulsive for the more neutron-rich fragments, which would lead to a positive slope, more positive in the asy-soft case. Combining the two effects, the final slope can be positive or negative, it should increase for asy-soft EOS and neutron-rich systems. This is well observed in the figure, where the steeper

[16] Fragments are defined by applying a coalescence procedure to matter with density larger than $\rho_0/5$

[17] N/Z of fragments is defined as the average over the number of events of the ratio $\sum_i N_i / \sum_i Z_i$, the sums running on all fragments i with charge between 3 and 10 contained in each event.

negative slope is for the asy-stiff EOS and the less neutron-rich system (^{112}Sn), and the more positive is for the neutron richer system, ^{132}Sn. The right panel shows that the observed effects are still present for the cold fragments.

Studies using this variable are in progress by the MSU group and by the INDRA collaboration (thesis of F. Gagnon-Moisan). The MSU results can again be interpreted differently, depending on the transport code used: while with ImQMD they show a better agreement between data and an asy-soft EOS (γ ~0.5)[18], they better match with an asy-stiff EOS (γ ~1.6) with the BNV [44] code[19]. The INDRA data are still preliminary, and seem to qualitatively favour an asy-stiff EOS. Calculations for the measured systems (^{136}Xe +^{124}Sn and ^{124}Xe+^{112}Sn at 32 and 45 A MeV) are in progress.

8 Neck fragmentation at Fermi energies

As said above (sect.3.2), for a large fraction of the reaction cross section at energies 15-50 A MeV the exit channel of the collisions comprise several light products (Z<10) emitted in the interaction zone, with a velocity intermediate between those of the two main partners. These reactions are characterized by the alignment of the velocity vectors of QP, QT and neck fragments: in the reaction plane the

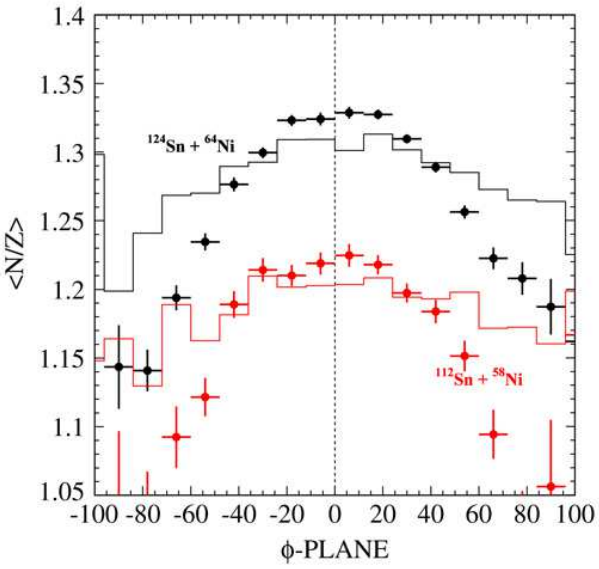

Figure 22: Average N/Z of neck fragments vs their in-plane emission angle, for ternary events measured for two Sn+Ni reactions at 35 A MeV. The lines represent the distribution of all IMF whereas the points concern fast emitted fragments (sequential fission removed). From [45].

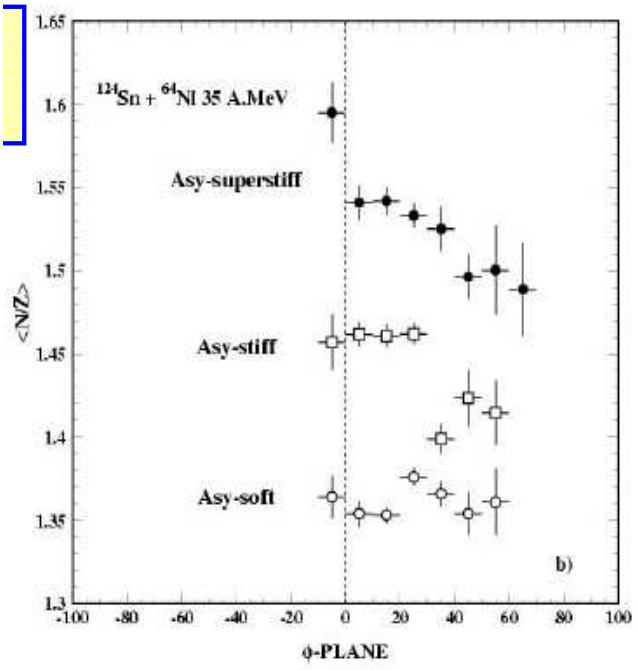

Figure 23: Same as fig 22 for the N/Z of hot fragments obtained in stochastic BNV simulations. From E. De Filippo, NUFRA2007.

angular distributions of the latter have a maximum at $\Phi_{plane} = 0$, Φ_{plane} being the angle between the

[18] see the talk of B. Tsang at the NUFRA 2009 conference: http://fias.uni-frankfurt.de/historical/nufra2009
[19] talk of H. Wolter at the IWM2009 workshop, http://agenda.ct.infn.it/contributionListDisplay.py?confId=128

QP-QT separation axis and the velocity of the neck fragment. This phenomenon has been known and studied for two decades [46–48]. The good isotopic resolution of the CHIMERA array allows to study the isospin content of the neck fragments. These clusters are expected to be formed in a slightly dilute zone, $\rho_0/2 < \rho < \rho_0$, in contact with the normal density regions of QP/QT. Isospin transport effects due to the drift coefficient are expected. Fig.19 shows that in this region protons and neutrons move now in opposite directions: neutrons towards the low density neck region and protons towards the QP/QT zones. Because of the larger slope of the chemical potential, a larger neutron flow is expected with an asy-stiff EOS. The neck fragments should thus be very neutron-rich, even more than those produced in the gas-phase through isospin distillation.

The Isospin Collaboration studied the isospin content of the neck fragments as a function of their degree of alignment, for two reactions ^{124}Sn+^{64}Ni and ^{112}Sn+^{58}Ni. They observed that the N/Z presents a maximum value when the fragments are exactly aligned with the QP and QT. This maximum better shows up when fragments arising from sequential fission are removed: compare the points in the figure (only aligned fragments) with the lines (all fragments). The maximum is also more marked for the neutron-richer system. The same analysis was performed on results from stochastic BNV simulations, using three forms of the potential symmetry energy. The results are displayed in fig 23 [20]. The value of N/Z is rather flat for an asy-soft EOS, and one should take a stiff asy-EOS in order to observe a maximum of the N/Z value for $\Phi_{plane} = 0$. Although only partial (no de-excitation of neck fragments in BNV), this comparison calls for an asy-stiff EOS ($\gamma \in [1, 1.6]$).

9 Neutron skin

It has long been known that in stable heavy nuclei neutron and proton densities differ, particularly by their root-mean-square radii. The neutron rms radius appears as an ideal quantity for constraining

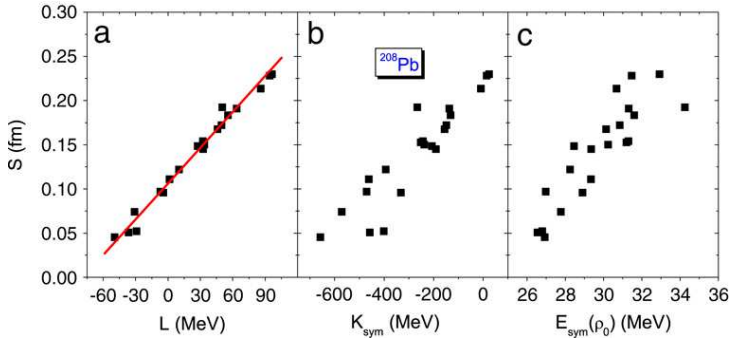

Figure 24: Neutron skin thickness, S, of ^{208}Pb as a function of (a) L, (b) K_{sym} and (c) $E_{sym}(\rho_0)$ for 21 sets of Skyrme interaction parameters. The line in panel (a) represents a linear fit. From [49]

the symmetry energy part of the EOS. Using Skyrme parameterizations of the nuclear interaction, it can be shown that the neutron skin thickness, S [21], depends on the symmetry energy around normal density, The dependence of S on the various terms of the expansion, Eq.6 is shown in fig. 24, for 21

[20] Warning: this figure gives the N/Z of excited neck fragments

[21] defined as $S = \sqrt{\langle r_n^2 \rangle} + \sqrt{\langle r_p^2 \rangle}$

different Skyrme parameterizations [22]. It is observed that S is linearly correlated with the slope L of the symmetry energy at normal density and more loosely related to the other parameters K_{sym} and $E_{sym}(\rho_0)$. S is unfortunately difficult to measure in a model-independent way, and the scarce results were obtained with a poor accuracy. Neutron skin thicknesses would be all the more interesting to know that they were related to the crust of neutron stars, which is also made of neutron-rich nuclear matter. The collective vibration of the excess neutrons of the skin against the bulk symmetric matter is at the

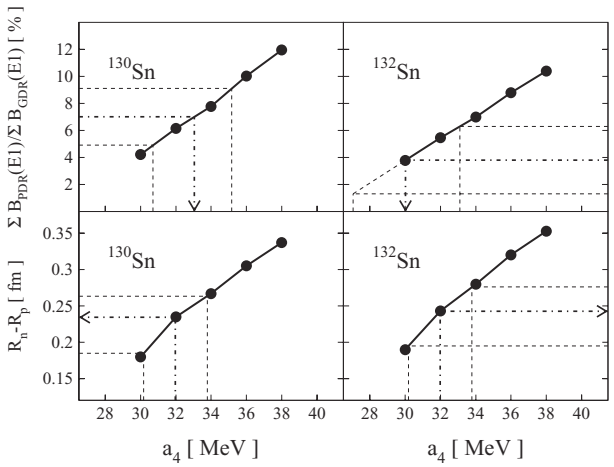

Figure 25: Upper panels: ratio of pygmy to giant dipole resonance strength for$^{130,132}Sn$ versus the symmetry energy parameter a_4 as resulting from RQRPA calculations (solid lines). The dot-dashed and dashed lines indicate the experimental PDR/GDR strength ratios with their errors and the range of a_4 values deduced from them. Bottom panels: neutron skin thickness $R_n - R_p$ versus a_4 from RQRPA calculations The dot-dashed and dashed lines indicate the average a_4 value and its errors and the neutron-skin thicknesses deduced from it. From [50]

origin of the pigmy dipole resonance, with a transition energy below that of the giant dipole resonance. It was recently proposed that the strength of the pigmy resonance could also provide a constraint on the symmetry energy. In [50] a series of self-consistent relativistic Hartree-Bogoliubov model plus relativistic quasiparticle random phase approximation (RQRPA) calculations of ground-state properties and dipole strength distributions was carried out. The value of $E_{sym}(\rho_0)$ in the used effective interactions was varied between 30 and 38 MeV and the other parameters adjusted to reproduce the nuclear matter properties. With such consistent calculations, a direct relation between symmetry energy parameters, neutron skin and pygmy resonance strength can be obtained. This is exemplified in fig 25 for ^{130}Sn and ^{132}Sn, which shows that the pigmy strength is linearly correlated to the neutron skin and to $E_{sym}(\rho_0)$ (noted a_4 in the figure). The measured ratio of the PDR and GDR strengths is compared to that of the RQRPA calculations, which fixes the symmetry energy parameters:

$$a_4 = 32.0 \pm 1.8 \text{ MeV and } L = 43 \pm 15 \text{ MeV}$$

This parametrization corresponds to a soft asy-EOS, with $\gamma \in [0.3; 0.5]$

10 Constraint on the EOS at supra-saturation density

10.1 n, p collective flows

In central nuclear collisions at incident energies larger than ~200 A MeV baryon densities of the order of 2-3 ρ_0 can be reached, providing a way to test the symmetry energy at suprasaturation densities. The neutron and proton differential flows are good probes of the compressed stage of of the collisions. The

[22] SKM, SKM*, RATP, SI, SII, SIII, SIV, SV, SVI, E, E_σ, G_σ, R_σ, Z, Z_σ, Z^*_σ, T, T3, SkX, SkXce and SkXm, see [3] for the parameters used in these interactions.

flow observables are expressed as the 1^{st} and 2^{nd} coefficients of the Fourier expansion of the azimuthal distribution of particles:

$$\frac{\mathrm{d}N}{\mathrm{d}\phi}(y, p_t) = 1 + v_1 \cos(\phi) + 2v_2 \cos(2\phi)$$

v_1 characterizes the transverse flow, related to the azimuthal anisotropy of the transverse nucleon emission. v_2 characterizes the elliptic flow, describing the competition between in-plane and out-of-plane emissions: in-plane emission is favoured for $v_2 > 0$ whereas $v_2 < 0$ is obtained for out-of-plane emission (squeeze-out).

Measurements of flow observables from Au+Au reactions at 400 AMeV were performed at GSI, using the FOPI and LAND apparatuses [51]. In a new and recent analysis of these data, combined data sets for central and mid-peripheral collisions were compared with the results of UrQMD calculations [23], with two

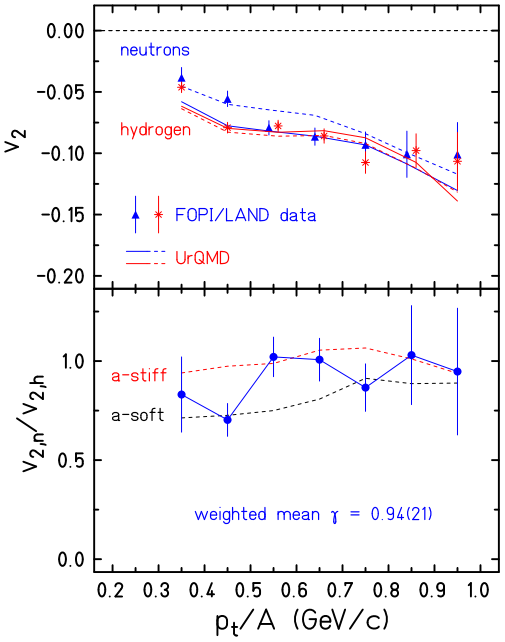

Figure 26: Differential elliptic flow parameters ν_2 for neutrons (triangles) and hydrogens (stars), top panel, and their ratio (bottom panel) for central (b <7.5 fm) collisions of ^{197}Au+^{197}Au at 400 AMeV as a function of the transverse momentum per nucleon p_t/A. The symbols represent the experimental data, the UrQMD predictions for γ=1.5 (asy-stiff) and 0.5 (asy-soft) are given by the dashed lines. From [52].

parameterizations of E_{sym}^{pot}, corresponding to γ values 0.5 and 1.5. Fig. 26 shows the evolution of ν_2 for neutrons and hydrogens [24] as a function of the transverse momentum, p_t. The upper panel of the figure shows that the model (lines) well describes the overall dependence of the experimental data (points). It appears that the neutron squeeze-out is significantly sensitive to the symmetry energy whereas that of hydrogens is not. As a consequence the squeeze-out ratio, displayed in the bottom panel of the figure is a good probe of the stiffness of the symmetry energy. The results however suffer a lack of statistics and the points present a large dispersion. A linear interpolation between the two calculations, averaged over the range of transverse momentum 0.3-1.0 GeV/c, yields the estimate $\gamma \approx 0.9 \pm 0.3$.

It must be noted that a new experiment aiming at measuring these flows will be realized at GSI within two years. The experimental set-up will combine LAND with parts of CHIMERA and the ALADIN time-of-flight wall.

[23] performed for $b < 7.5$ fm and filtered by FOPI/LAND acceptances
[24] protons, deuterons and tritons are summed

10.2 Meson production at supra-saturation density

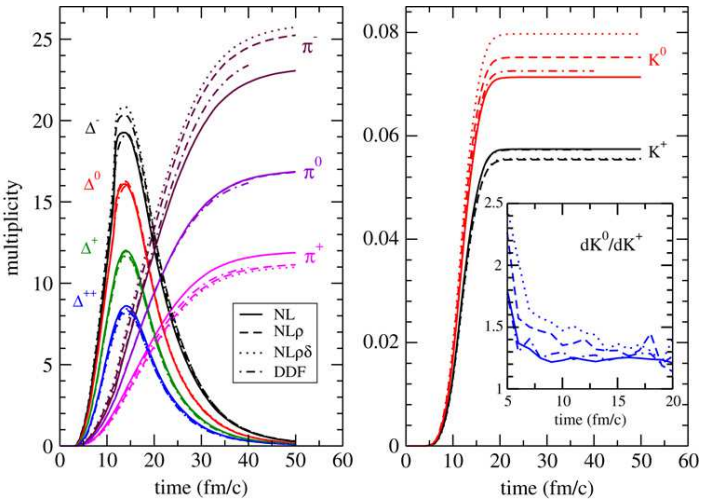

Figure 27: Time evolution of the $\Delta^{\pm,0,++}$ resonances and pions $\pi^{\pm,0}$ (left), and kaons $K^{+,0}$ (right) for a central (b=0 fm impact parameter) Au+Au collision at 1 A GeV incident energy. Transport calculations using the NL, $NL\rho$, $NL\rho\delta$ and DDF models for the isovector part of the nuclear EOS are shown. The inset contains the differential K^0/K^+ ratio as a function of the kaon emission time. From [45].

At high energies, the meson production proved to be a reliable observable to probe the EOS at high density. Thus the isospin content of the mesons can be expected to provide information on the symmetry energy at high density. In a Relativistic Mean Field approach, pion and kaon productions in head-on Au+Au collisions at 1 A GeV [45] were calculated. The relativistic Landau-Vlasov method was applied together with a Monte-Carlo procedure for hard hadron collisions. The inelastic channels in the collision term involve the production and absorption of the Δ and N^* resonances[25] and their decay into pions. Depending on the isovector meson contributions, the models are termed NL, $NL\rho$ and $NL\rho\delta$,

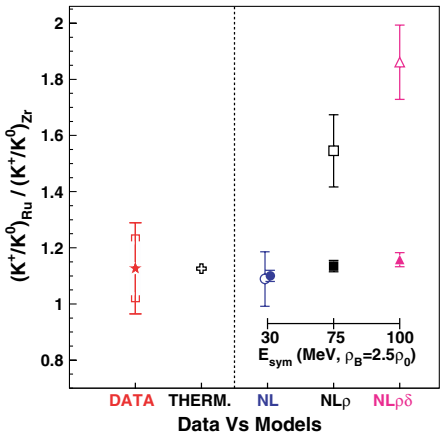

Figure 28: Experimental ratio $(K^+/K^0)_{Ru}/(K^+/K^0)_{Zr}$ (stars) and theoretical predictions of the thermal model (cross) and the transport model with three different assumptions on the symmetry energy: NL (circles), $NL\rho$ (squares), and $NL\rho\delta$ (triangles), for two sets of calculations: INM (open symbols) and HIC (full symbols). Statistic ans systematic errors are represented by vertical bars and brackets respectively. From [53].

in increasing order of asy-stiffness. Fig. 27 shows the evolution with time of the multiplicities of Δ, pions ans kaons. It is clear that kaons should be better probes of the high density stage as they are all produced in the very first instants of the collision. Conversely pions are produced and re-absorbed during a longer time. The π^- yield slightly increases when increasing the vector contribution in the

[25] The energies of the Δ is 1232 MeV and that of the N^* 1440 MeV

isovector channel ($NL \rightarrow NL\rho\delta$), while that of π^+ barely decreases. The effect is more marked on kaons, especially on K^0.

The production of kaons was experimentally measured for $^{96}_{44}$Ru+$^{96}_{44}$Ru and $^{96}_{40}$Zr+$^{96}_{40}$Zr collisions at 1.5 A GeV, using the FOPI detector [53]. These systems have the same mass but different isospins. The measured double ratio of K^+/K^0 is shown in fig. 28 by the red star. It is compared to the results of RMF calculations of nuclear collisions (close circle, square and triangle). At that energy, and in view of the large experimental error bars, no information on E_{sym} can be obtained.

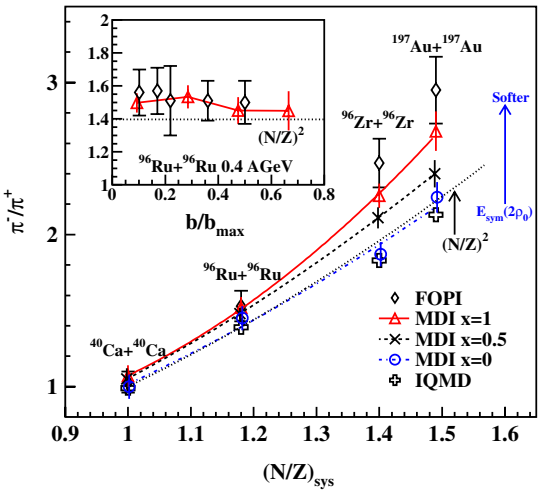

Figure 29: The π^-/π^+ ratio as a function of the neutron/proton ratio of the reaction system at 0.4 A GeV with the reduced impact parameter of b/b_{max} $\leq$0.15. The inset is the impact parameetr dependence of the π^-/π^+ for the ^{96}Ru+^{96}Ru reaction at 0.4 A GeV. From[54]

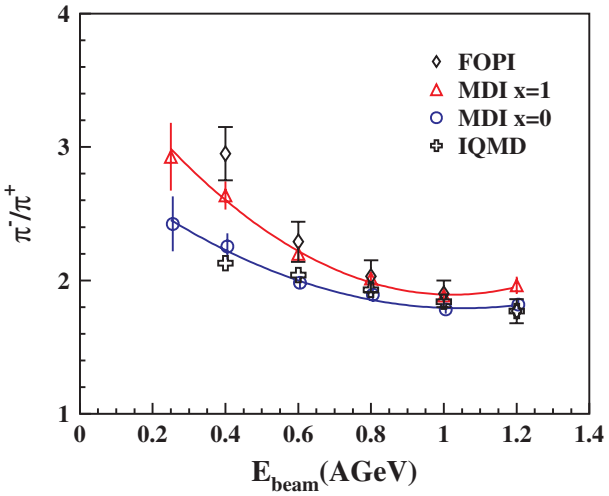

Figure 30: Excitation function of the π^-/π^+ ratio in the most central Au+Au collisions. From[54]

The FOPI collaboration also measured the pions production for symmetric systems ranging from Ca+Ca to Au+Au at energies between 0.2 and 1.2 A GeV. Results were analysed for central collisions, where the estimated density is around $2\rho_0$ [55]. Fig. 29 shows the π^-/π^+ ratio obtained at 400 A MeV versus the N/Z of the different colliding systems and fig. 30 displays the excitation function of the pion ratio for the Au+Au system. They are compared with the predictions of the IBUU04 model with different symmetry energies, and with those of the IQMD model. It is visible that the result can discriminate between the EOS for systems with large N/Z (Zr+Zr and Au+Au), and for moderate incident energies, close to the π production threshold. In this framework of isospin and momentum-dependent transport model, a very soft EOS ($x > 1 \equiv \gamma < 0.3$) is favoured at high density [54]. This surprising result may be the indication that there are limitations on what can be reliably learnt about $E_{sym}(\rho)$ at high density from high energy heavy-ion collisions.

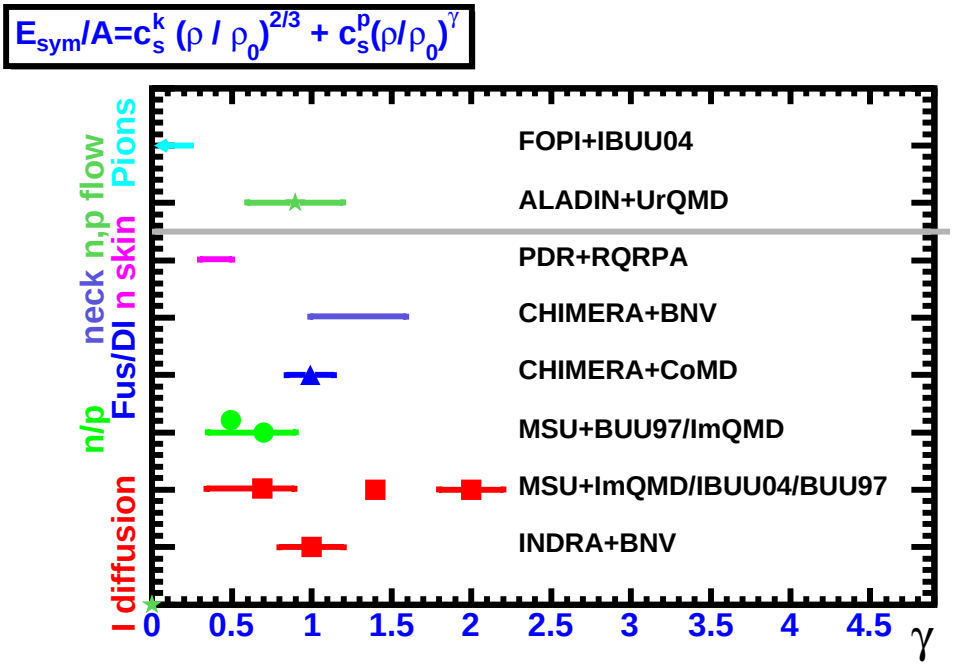

Figure 31: Summary of the experimental findings. Several points on the same horizontal position correspond to γ extracted from different codes, in the same left-to-right order. The horizontal line separates "low density" from "high density" results.

11 Summary of the results

We summarize in fig. 31 the values of γ derived from the different experiments presented in this lecture. Except the very first result from MSU obtained with BUU97, they at most equal to 1.5, indicating that the symmetry energy should not be very stiff. The asy-stiffness is found softer with the ImQMD code than with mean-field codes. Two results point towards a very asy-soft-EOS (those from neutron skin and pions). Clearly more results are needed, on both the experimental and the theoretical side.

12 Discussion: problems raised and possible improvements

In the course of this lecture, some difficulties for obtaining the symmetry energy evolution with density from comparison between experimental data and models have been raised. They will be summarized here, together with some foreseen improvements, both on the experiments and in the models.

It must be stressed that the expected isospin effects being small, a high experimental statistics is mandatory to minimize, at least, the statistical error on the measured variables; some of the presented results exhibit indeed quite large error bars.

12.1 Impact parameter selection

Transport codes simulate collisions at a given impact parameter, b, a quantity which is not known experimentally. Some global variables [26] are often used to get an experimental impact parameter, b_{exp} [24]. Due however to the limitations of the measurements (less than the reaction cross section is generally recorded, which means $b_{exp}^{max} < b^{grazing}$), and to the large fluctuations in the mechanisms occurring at a given impact parameter, there is not a one-to-one correspondence between b and b_{exp}. This may cause some uncertainty in the symmetry energy derived from a comparison with a transport code at a given impact parameter.

An appealing procedure to partially get rid of these problems is to treat experimental and simulated data on the same footing: for instance one can use the same b-dependent global variable as a sorting parameter for experimental data and model, as done for the results presented in sections 4 and 5.3.

12.2 Complete identification of the fragments

In several cases the choice of the stiffness of the symmetry energy relies on the measurement of the N/Z of the fragments. This implies that, besides the energy and the charge, one should measure the masses of the fragments. With the presently existing detectors, the isotopic resolution is obtained up to Z=9 and on a limited solid angle. Even the CHIMERA array, with its time-of-flight, has difficulties in obtaining both Z and A for the heavier fragments. It would be desirable to know the higher masses, and particularly that of the heaviest fragment of the partitions (see section 2.5).

In this aim the FAZIA collaboration carries on an ambitious research and development program, which should end-up in building a new 4π array. It is based on pulse-shape identification of nuclei in silicon detectors and scintillators, thanks to a fully digitized electronics [27].

12.3 Transport codes

12.3.1 In-medium effects

It was underlined in section 3.1 that there was often a lack of internal consistency between the mean-field and the collision terms. Indeed the in-medium corrections to be applied to the collision term are not well known. In the same line the in-medium effects on the production, absorption, propagation pf π, K are not well known.

12.3.2 Comparison between experiment and simulations

The results displayed in sections 5.2 and 6, which present comparison of the same experimental data with those of different transport codes prove that the form of the symmetry energy term of the EOS is far from being settled. A comparative study of the codes, in the spirit of that initiated by the WCI [56] for the isoscalar EOS, would be desirable. Among others, some points to be studied are the following: (i) the effect of momentum dependent interactions which, besides increasing the amount preequilibrium emission [43] may also influence the balance between that emission and isospin diffusion, which occur simultaneously. (ii) improvements of the codes towards more consistency between mean field and collision

[26] A global variable condense all the information recorded per event in a single value. Some commonly used variables are multiplicities (of neutrons, of charged products, of light charged particles), transverse energies, total detected charge, dissipated energy.

[27] http://fazia.in2p3.fr

term should be looked for. (iii) the quantal nature of the nuclear systems should be preserved. Besides AMD and FMD, the DYWAN code, based on algorithms using wavelets [57], could bring new interesting information for heavy systems. The codes should also be as predictive as possible.

12.4 From hot to cold fragments

Experimentally we measure fragments long after the end of the collision. They are thus cold fragments, having lost their possible excitation energy through evaporation (or fission). As mentioned in section 3.1 the semi-classical nature of most of the transport codes does not allow them to follow the de-excitation process of the nuclei present in the exit channel. Similarly in statistical models for multifragmentation the calculated partitions at freeze-out deal with hot fragments. A de-excitation code (sometimes termed after-burner) must thus be used, following both types of models, before any comparison with data. One can wonder about the reliability of the statistical de-excitation codes: the GEMINI [58] is widely used. The SIMON code [59] used in Europe has the advantage of keeping space-time correlations while de-exciting the fragments. The MSU group developed a statistical multifragmentation model in which the de-excitation part wss also improved [60].

Indeed the only validations of decay codes which could be performed up to now consisted in studying the de-excitation of compound nuclei, formed with stable beams and targets; the compound nuclei are thus slightly neutron-deficient, owing to the curvature of the valley of stability. The hot fragments formed in multifragmentation might be more neutron-rich (if they keep the N/Z of the fragmenting system), as well as more neutron-deficient; the isospin dependence of the level density parameter is largely unknown when approaching the drip-lines. To get more stringent experimental constraints the INDRA collaboration initiated a program of fully exclusive measurements (the evaporation residue and all the emitted harged products are measured in coincidence): the de-excitation of Pd compound nuclei with masses ranging from 92 to 104 and excitation energies around 3 A MeV [61] and the yield of light fragment evaporation from Ba compound nuclei [62].

These codes, when based on the Weiskopff theory, rely on the assumption that the hot residue has time to re-arrange between two successive evaporations. This hypothesis is violated when the excitation energy reaches high values, due to the very short emission time [63]. It was shown recently that fragments issued from multifragmentation are indeed excited up to 3-3.5 A MeV [64, 65].

De-excitation weakens the expected isospin effects. This has been well evidenced in the isospin diffusion study of the INDRA collaboration [38]. There is unfortunately no remedy to that fact. One can however hope to increase isospin effects by enlarging the explored N/Z range, thanks to the availability of new radioactive beams.

13 Conclusion

As stressed in ref. [36], more strength is given to a symmetry energy term if several different experimental variables can be well accounted for with it. This was accomplished by studying isospin diffusion and n/p double ratios in the same Sn+Sn experiments within the ImQMD framework. In Europe one could imagine comparing various results obtained with INDRA and CHIMERA with those of a single version of the stochastic BNV code of the Catania group. One can also wonder to what extent the differences in γ values obtained when comparing experiments to different models are due to the transport code itself (hot fragments), or to the secondary decay model. Finally the availability of more exotic beams should help to progress, by enlarging the range of explored N/Z.

A Glossary of the transport codes

Acronym	*Full name*	Ref.	*Model*
BUU	Boltzmann Uehling Uhlenbeck	[66]	Simulations
VUU	Vlasov Uehling Uhlenbeck	[67]	of the nuclear
LV	Landau Vlasov	[68]	Boltzmann
BNV	Boltzmann Nordheim Vlasov	[69]	equation
BL	Boltzmann Langevin	[70]	Stochastic extension
SMF	Stochastic mean field	[71]	of Boltzmann equation
QMD	Quantum Molecular Dynamics	[72]	Classical
IQMD	Isospin QMD	[73]	A-body
UrQMD	Ultra relativistic QMD	[74]	
ImQMD	Improved Molecular Dynamics	[75]	
CoMD	Constrained Molecular Dynamics	[31]	models
FMD	Fermionic Molecular Dynamics	[76]	Molecular dynamics
AMD	Antisymmetrized Molecular Dynamics	[77]	with antisymmetrization

Table 2: Glossary of transport models used in the following sections. (Adapted from [28]).

B 4π arrays

The 4π arrays used for the experiments quoted in this paper, mostly at beam energies below 100 A MeV, are described in details in [78]. We will just mention here their principal characteristics. Among those

Array	Main location	number of modules	geometrical coverage	telescope
Miniball+LASSA[28]	MSU	188	80%	Plastic-CsI(Tl) + Si-Si-CsI(Tl)
Microball	Washington U.	95	97%	CsI(Tl)
INDRA	GANIL	336	90%	IoCh-Si-CsI(Tl)
CHIMERA	LNS Catania	1192	94%	Si-CsI(Tl); ToF

Table 3: Principal 4π charged product detectors. The geometrical coverage is expressed in percent of the 4π solid angle. IoCh stand for ionization chamber and ToF for time of flight measurement.

only INDRA and CHIMERA are able to identify the heaviest fragments, with atomic numbers $Z \geq 18$.

At energies above 100 A MeV, the cited data were recorded with two detection ensembles:

- FOPI (FOur π) comprises a superconductor solenoid, a forward plastic wall, forward and central drift chambers and a plastic barrel. It detects and identify all charged products of a nuclear reaction.
- ALADIN is a spectrometer, coupled with a TP chamber, a time-of-flight wall. It detects and identifies charged products - except the hydrogen isotopes- emitted by the quasi-projectile produced

[28] The 9 modules of LASSA, coupled with the miniball, provide good isotopic and angular resolutions over a limited solid angle

in a collision. When complemented with a neutron wall, LAND (Large Area Neutron Detector), it gives neutron multiplicity and energy in a forward solid angle;

C Acknowledgements

Many thanks to Bernard Borderie, Maria Colonna, Emmanuelle Galichet and Paolo Napolitani for illuminating discussions.

References

[1] V. Baran, M. Colonna et al., *Phys. Rep.* **410** (2005) 335.

[2] Bao-An Li, Lie-Wen Chen and Che Ming Ko, *Phys. Rep.* **464** (2008) 113.

[3] P. Danielewicz and J. Lee, *Nucl. Phys.* **A 818** (2009) 36.

[4] W. D. Myers and W. J. Swiatecki, *Ann. Phys.* **55** (1969) 395.

[5] P. Moller, J. R. Nix et al., *At. Data Nucl. Data Tables* **59** (1995) 185.

[6] P. Chomaz, M. Colonna and J. Randrup, *Phys. Rep.* **389** (2004) 263.

[7] F. Gulminelli, *Ann. Phys. Fr.* **29** (2004) 1.

[8] D. H. E. Gross, *Rep. Prog. Phys.* **53** (1990) 605.

[9] A. H. Raduta and A. R. Raduta, *Phys. Rev.* **C 55** (1997) 1344.

[10] A. H. Raduta and A. R. Raduta, *Phys. Rev.* **C 65** (2002) 054610.

[11] J. Bondorf, A. S. Botvina et al., *Phys. Rep.* **257** (1995) 133.

[12] M. B. Tsang, W. A. Friedman et al., *Phys. Rev. Lett.* **86** (2001) 5023.

[13] H. Xu, M. B. Tsang et al., *Phys. Rev. Lett.* **85** (2000) 716.

[14] M. B. Tsang, W. A. Friedman et al., *Phys. Rev.* **C 64** (2001) 041603.

[15] M. B. Tsang, C. K. Gelbke et al., *Phys. Rev.* **C 64** (2001) 054615.

[16] Ad. R. Raduta and F. Gulminelli, *Phys. Rev.* **C 75** (2007) 024605.

[17] A. Le Fèvre, G. Auger et al. (INDRA and ALADIN Collaborations), *Phys. Rev. Lett.* **94** (2005) 162701.

[18] A. Ono, P. Danielewicz et al., *Phys. Rev.* **C 68** (2003) 051601.

[19] T. X. Liu, J. van Goethem et al., *Phys. Rev.* **C 69** (2004) 014603.

[20] C. Dorso, *Phys. Rev.* **C 73** (2006) 034605.

[21] M. Colonna and M. B. Tsang, P. Chomaz, F. Gulminelli et al. (eds.) Dynamics and Thermodynamics with nuclear degrees of freedom, Springer, 2006, vol. 30 of *Eur. Phys. J. A*, 165–182.

[22] Fu Yao and Fang De-Qing and Ma Yu-Gang and Cai Xiang-Zhou and Tian Wen Dong and Wang Hong-Wei and Guo Wei, *Chin. Phys. Lett.* **26** (2009) 082503.

[23] G. Lehaut, thèse de doctorat, Université de Caen (2009), http://tel.archives-ouvertes.fr/tel-00426878.

[24] B. Borderie and M. F. Rivet, *Prog. Part. Nucl. Phys.* **61** (2008) 551.

[25] B. A. Li, C. B. Das et al., *Phys. Rev.* **C 69** (2004) 011603.

[26] L. W. Chen, C. M. Ko and B. A. Li, *Phys. Rev. Lett.* **94** (2005) 032701.

[27] M. Prakash, T. L. Ainsworth and J. M. Lattimer, *Phys. Rev. Lett.* **61** (1988) 2518.

[28] E. Suraud, Nuclei in collision: lectures given at the Joliot-Curie school 1995, Editions de Physique, 1996, vol. 21 of *Ann. Phys. Fr.*, 461–502.

[29] J. P. Blaizot, D. Gogny and B. Grammaticos, *Nucl. Phys.* **A 265** (1976) 315.

[30] F. Amorini, G. Cardella et al., *Phys. Rev. Lett.* **102** (2009) 112701.

[31] M. Papa, T. Maruyama and A. Bonasera, *Phys. Rev.* **C 64** (2001) 024612.

[32] J. Rizzo, M. Colonna et al., *Nucl. Phys.* **A 806** (2008) 79.

[33] M. B. Tsang, T. X. Liu et al., *Phys. Rev. Lett.* **92** (2004) 062701.

[34] Bao-An Li, Che Ming Ko and W. Bauer, *Int. J. Mod. Phys.* **E 7** (1998) 147.

[35] Y. Zhang, P. Danielewicz et al., *Phys. Lett.* **B 664** (2008) 145.

[36] M. B. Tsang, Y. Zhang et al., *Phys. Rev. Lett.* **102** (2009) 122701.

[37] E. Galichet, M. F. Rivet et al. (INDRA Collaboration), *Phys. Rev.* **C 79** (2009) 064614.

[38] E. Galichet, M. Colonna et al., *Phys. Rev.* **C 79** (2009) 064615.

[39] T. Lefort, D. Doré et al. (INDRA Collaboration), *Nucl. Phys.* **A 662** (2000) 397.

[40] M. A. Famiano, T. Liu et al., *Phys. Rev. Lett.* **97** (2006) 052701.

[41] B.-A. Li, C. M. Ko and Z. Ren, *Phys. Rev. Lett.* **78** (1997) 1644.

[42] B.-A. Li, L.-W. Chen et al., *Phys. Lett.* **B 634** (2006) 378.

[43] V. Greco, A. Guarnera et al., *Phys. Rev.* **C 59** (1999) 810.

[44] M. Colonna, V. Baran et al., *Phys. Rev.* **C 78** (2008) 064618.

[45] M. Di Toro, V. Baran et al., *Prog. part. Nucl. Phys.* **62** (2009) 389.

[46] G. Casini, P. G. Bizetti et al., *Phys. Rev. Lett.* **71** (1993) 2567.

[47] J. Colin, D. Cussol et al. (INDRA Collaboration), *Phys. Rev.* **C 67** (2003) 064603.

[48] E. De Filippo, A. Pagano et al. (CHIMERA-ISOSPIN collaboration), *Phys. Rev* **C 71** (2005) 064604.

[49] L. W. Chen, C. M. Ko and B. A. Li, *Phys. Rev.* **C 72** (2005) 064309.

[50] A. Klimkiewicz, N. Paar et al., *Phys. Rev.* **C 76** (2007) 051603.

[51] Y. Leifels, T. Blaich et al. (FOPI Collaboration), *Phys. Rev. Lett.* **71** (1993) 963.

[52] W. Trautmann, M. Chartier et al., I. Iori and A. Tarentola (eds.) Proc. XLVII Int. Winter Meeting on Nuclear Physics, Bormio, Italy, Ricerca scientifica ed educazione permanente, 2009, `nucl-ex/0907.2822`.

[53] X. Lopez, Y. J. Kim et al. (FOPI Collaboration), *Phys. Rev.* **C 75** (2007) 011901.

[54] Z. Xiao, B.-A. Li et al., *Phys. Rev. Lett.* **102** (2009) 62502.

[55] W. Reisdorf, M. Stockmeier et al. (FOPI Collaboration), *Nucl. Phys.* **A 781** (2007) 459.

[56] P. Chomaz, F. Gulminelli et al. (eds.) vol. 30 of *Eur. Phys. J. A*, Springer, 2006.

[57] B. Jouault, F. Sébille and V. de la Mota, *Nucl. Phys.* **A 628** (1998) 119.

[58] R. J. Charity, M. A. McMahan et al., *Nucl. Phys.* **A 483** (1988) 371.

[59] D. Durand, *Nucl. Phys.* **A 541** (1992) 266.

[60] W. P. Tan, S. R. Souza et al., *Phys. Rev.* **C 68** (2003) 034609.

[61] P. Marini, M. F. Rivet et al., Proc. II Int. Workshop on Compound Nuclear Reactions, AIP Conference Proceedings, 2009, 0.

[62] E. Bonnet, J. P. Wieleczko et al., *Int. J. of Modern Phys.* **E 17** (2008) 2359.

[63] B. Borderie, *Ann. Phys. Fr.* **17** (1992) 349.

[64] S. Hudan, A. Chbihi et al. (INDRA Collaboration), *Phys. Rev.* **C 67** (2003) 064613.

[65] S. Piantelli, B. Borderie et al. (INDRA Collaboration), *Nucl. Phys.* **A 809** (2008) 111.

[66] G. F. Bertsch and S. Das Gupta, *Phys. Rep.* **160** (1988) 189.

[67] H. Kruse, B. Jacak et al., *Phys. Rev.* **C 31** (1985) 1770.

[68] C. Grégoire, B. Remaud et al., *Nucl. Phys.* **A 465** (1987) 317.

[69] A. Bonasera, F. Gulminelli and J. Molitoris, *Phys. Rep.* **243** (1994) 1.

[70] S. Ayik and C. Grégoire, *Phys. Lett.* **B 212** (1988) 269.

[71] P. Chomaz, M. Colonna et al., *Phys. Rev. Lett.* **73** (1994) 3512.

[72] J. Aichelin, *Phys. Rep.* **202** (1991) 233.

[73] C. Hartnack, R. K. Puri et al., *Eur. Phys. J.* **A 1** (1999) 151.

[74] S. A. Bass, M. Belkacem et al., *Prog. Part. Nucl. Phys.* **41** (1998) 255.

[75] N. Wang, Z. Li and X. Wu, *Phys. Rev* **C 65** (2002) 064608.

[76] H. Feldmeier, *Nucl. Phys.* **A 515** (1990) 147.

[77] A. Ono, H. Horiuchi and T. Maruyama, *Phys. Rev.* **C 47** (1993) 2652.

[78] R. T. de Souza, N. Le Neindre et al., P. Chomaz, F. Gulminelli et al. (eds.) Dynamics and Thermodynamics with nuclear degrees of freedom, Springer, 2006, vol. 30 of *Eur. Phys. J. A*, 275–291.